Title

Mantle Structure and Flow Across the Continent-Ocean Transition of the Eastern North American Margin: Anisotropic S-Wave Tomography

Journal

Geochemistry Geophysics Geosystems, 22(12)

ISSN

1525-2027

Authors

Brunsvik, Brennan R
Eilon, Zachary C
Lynner, Colton

Publication Date

2021-12-01

DOI

10.1029/2021gc010084

Geochemistry, Geophysics, Geosystems®

AGU ADVANCING EARTH AND SPACE SCIENCE

RESEARCH ARTICLE
10.1029/2021GC010084

Mantle Structure and Flow Across the Continent-Ocean Transition of the Eastern North American Margin: Anisotropic *S*-Wave Tomography

Brennan R. Brunsvik[1], Zachary C. Eilon[1], and Colton Lynner[2]

[1]Department of Earth Science, University of California, Santa Barbara, CA, USA, [2]Department of Earth Sciences, University of Delaware, Newark, DE, USA

Key Points:

- We conducted mantle-scale velocity-anisotropy tomography across the continent-ocean transition of eastern North America
- The results capture layers of anisotropy preserved from collision and extension, as well as produced from modern mantle flow
- The imaged lithospheric and asthenospheric structure supports small-scale convection and margin parallel asthenospheric flow

Supporting Information:

Supporting Information may be found in the online version of this article.

Correspondence to:

B. R. Brunsvik,
brennanbrunsvik@ucsb.edu

Citation:

Brunsvik, B. R., Eilon, Z. C., & Lynner, C. (2021). Mantle structure and flow across the continent-ocean transition of the eastern North American margin: Anisotropic *S*-wave tomography. *Geochemistry, Geophysics, Geosystems*, *22*, e2021GC010084. https://doi.org/10.1029/2021GC010084

Received 5 AUG 2021
Accepted 14 NOV 2021

Abstract Little has been seismically imaged through the lithosphere and mantle at rifted margins across the continent-ocean transition. A 2014–2015 community seismic experiment deployed broadband seismic instruments across the shoreline of the eastern North American rifted margin. Previous shear-wave splitting along the margin shows several perplexing patterns of anisotropy, and by proxy, mantle flow. Neither margin parallel offshore fast azimuths nor null splitting on the continental coast obviously accord with absolute plate motion, paleo-spreading, or rift-induced anisotropy. Splitting measurements, however, offer no depth constraints on anisotropy. Additionally, mantle structure has not yet been imaged in detail across the continent-ocean transition. We used teleseismic *S*, *SKS*, *SKKS*, and *PKS* splitting and differential travel times recorded on ocean-bottom seismometers, regional seismic networks, and EarthScope Transportable Array stations to conduct joint isotropic/anisotropic tomography across the margin. The velocity model reveals a transition from fast, thick, continental keel to low velocity, thinned lithosphere eastward. Imaged short wavelength velocity anomalies can be largely explained by edge-driven convection or shear-driven upwelling. We also find that layered anisotropy is prevalent across the margin. The anisotropic fast polarization is parallel to the margin within the asthenosphere. This suggests margin parallel flow beneath the plate. The lower oceanic lithosphere preserves paleo-spreading-parallel anisotropy, while the continental lithosphere has complex anisotropy reflecting several Wilson cycles. These results demonstrate the complex and active nature of a margin which is traditionally considered tectonically inactive.

Plain Language Summary North America was once connected to Africa, but the continents rifted apart and are now separated by the Atlantic Ocean. The nature of rifting on land has been thoroughly studied. However, it is much more difficult to study the offshore region where the thinned continent pinches out and the tectonic plate transitions to sea-floor produced after continental breakup. Using a new data set from ocean-bottom seismic stations, we construct a 3-D image of seismic wavespeeds, which are diagnostic of rock type and temperature. We also image seismic anisotropy, which is the directional dependence of seismic velocity. Anisotropy is often used as a proxy for the orientation of stretching or mantle flow. We find wavespeed anomalies diagnostic of mantle upwelling associated with the shape and movement of the plate at the continent-ocean transition. The anisotropy model suggests that, in this region, the mantle beneath the plates is currently flowing along the margin. Within the tectonic plates, the mantle preserves anisotropy developed during cycles of rifting and collision. These seismic wavespeed and anisotropy models demonstrate the complex and active nature of a continental margin that is traditionally considered tectonically inactive.

1. Introduction

Continental rifting (e.g., McKenzie, 1978; Wernicke, 1985) and sea-floor spreading (e.g., Hess, 1962; Vine & Mathews, 1963) are fundamental tectonic processes. The transition from continental rifting to the production of seafloor and thus continental drifting, however, remains unclear (e.g., Begg et al., 2009; Crosby et al., 2008; Huismans & Beaumont, 2011; Kendall et al., 2005; Larsen et al., 2018; Shillington et al., 2006; Van Avendonk et al., 2006; X. Yuan et al., 2017). Seismic resolution across the rift-drift transition, particularly in the mantle, is extremely limited due to the sparsity of broadband ocean-bottom seismometers (OBSs) offshore at rifted margins.

The eastern North American passive margin (ENAM) is an excellent location to study the tectonics of the rifted continent-ocean transition (COT). ENAM is a mature passive margin resulting from the rifting of Pangaea at ~230-200 Ma (Withjack et al., 2012). There has been relatively little deformation at ENAM since the transition

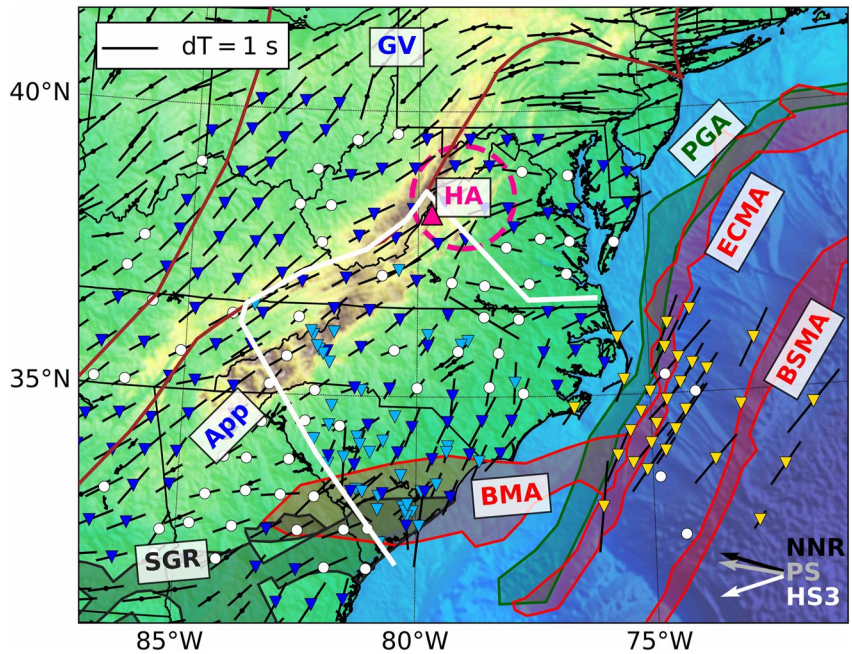

Figure 1. Map of the study area, showing stations used in our inversion (inverted triangles and white circles) and previous splitting measurements (Long et al., 2016; Lynner & Bodmer, 2017; Yang et al., 2017) that we averaged at each station. Splitting measurements are black lines centered at stations. Stations with dominantly null splitting are white circles. These null splitting stations had quality null arrivals and no split arrivals in Lynner and Bodmer (2017) and Long et al. (2016), but may still have split arrivals in Yang et al. (2017). For non-null splitting stations, the OBSs and land stations that were deployed as part of the ENAM-CSE are yellow triangles, the TA is dark blue triangles, and other networks are light blue triangles. The white line shows the boundary between stations where we measured splitting and stations where we only measured differential travel times. We also show splitting averages outside our seismometer array, where stations are indicated as small black dots. The Appalachian (App) and Grenville (GV) province boundaries are indicated by brown lines. The low velocity Harrisonburg anomaly (HA) is indicated with a pink, dashed circle (HA location is from our results; see also Biryol et al., 2016; Pollitz & Mooney, 2016; Savage, 2021). The pink triangle is the approximate location of Eocene volcanics (Mazza et al., 2014). Arrows at bottom right show approximate orientations of paleo-spreading (PS) (Becker et al., 2014) and plate-motion in no-net-rotation (NNR; DeMets et al., 2010) and hot-spot (HS3; Gripp & Gordon, 2002) reference frames. We highlighted the Positive Gravity Anomaly (PGA) based on Sandwell and Smith (2009). We highlighted magnetic anomalies (BMA, ECMA, BSMA) based on Maus et al. (2009). South Georgia Rift basin (SGR) modified from Akintunde et al. (2014) and Chowns and Williams (1983). OBSs: ocean-bottom seismometers. ENAM-CSE: Eastern North American margin community seismic experiment. TA: Transportable Array. HA: Harrisonburg anomaly. SGR: South Georgia Rift basin. App: Appalachian. GV: Grenville province. BMA: Brunswick Magnetic Anomaly. PGA: Positive Gravity Anomaly. ECMA: East Coast Magnetic Anomaly. BSMA: Blake Spur Magnetic Anomaly. PS: Paleo-spreading orientation. NNR: No-net-rotation reference frame. HS3: Hot-spot reference frame.

from rifting to continental drifting in the Jurassic (Schlische, 2003; Withjack & Schlische, 2005). Structures associated with rifting along the margin are thus likely unperturbed and can offer insights into rifting processes.

ENAM is a natural laboratory for studying rifting processes (Worthington et al., 2021). It was selected as a primary site for a Geodynamic Processes at Rifting and Subducting Margins (GeoPRISMS) community seismic experiment (CSE) (Lynner et al., 2020). Thirty broadband OBSs were deployed in 2014–15, while the Transportable Array (TA) was in the eastern US (Figure 1). The TA provided excellent on-land broadband seismic coverage in the eastern US throughout 2012–2015, supporting interrogation of the continent. Combined, the ENAM-CSE and TA provide dense, co-temporal seismic data coverage crossing the COT. The ENAM-CSE constitutes one of the only rifted-margin crossing broadband OBS datasets, which is capable of interrogating a rifted COT in the mantle. This data set has already been utilized for crustal-scale ambient noise tomography (C. Li & Gao, 2021; Lynner & Porritt, 2017), shear-wave splitting analyses (Lynner & Bodmer, 2017), multi-channel reflection imaging (Bécel et al., 2020), and crustal to uppermost-mantle tomography based on wide-angle seismic data (Shuck et al., 2019). However, no margin-spanning body-wave velocity or 3-D anisotropy models have been developed

that illuminate the offshore mantle with the coverage offered by these OBSs, leaving mantle structure and flow across the COT largely unknown.

1.1. The ENAM Continent-Ocean Transition

During continental breakup, the lithosphere thins (e.g., Crosby et al., 2008; Huismans & Beaumont, 2011; Wernicke, 1985; Ziegler & Cloetingh, 2004). However, it is unknown whether there is a transition in plate thickness, wavespeed, or other properties across the ENAM COT. It is not known whether the lithosphere-asthenosphere boundary (LAB) bears a signature of the COT (e.g., X. Yuan et al., 2017) because the lithospheric and mantle structure at the COT has not been imaged in detail.

Several studies have used dense on-land seismic coverage to image the ENAM continental crust and mantle (e.g., Bedle & van der Lee, 2009; Biryol et al., 2016; Forte et al., 2007; Golos et al., 2018; Guo et al., 2019; Pollitz & Mooney, 2016; Savage, 2021; Savage et al., 2017; Schmandt & Lin, 2014; van der Lee et al., 2008; Wagner et al., 2018). These informed the continent's lithospheric structure, which contains a mid-lithospheric discontinuity in the continental interior, thins toward the ocean, and is highly thinned at the Harrisonburg anomaly (HA) in Virginia (e.g., Abt et al., 2010; Byrnes et al., 2019; Savage, 2021). However, studies to date have focused primarily on continental structures and have not incorporated the new OBS data.

Utilizing ENAM-CSE OBSs, recent Rayleigh wave ambient noise phase velocity tomography has shown crustal thinning across the margin and a correlation between the East Coast Magnetic Anomaly (ECMA) and a region of thinned crust (Lynner & Porritt, 2017). Full-waveform ambient-noise tomography reinforced these results (C. Li & Gao, 2021). The presence of the ECMA at the edge of the margin suggests that it is correlated with the first oceanic material emplaced after rifting. Active source results show that the crust is thin (down to about 6–8 km) and highly faulted between the ECMA and the Blake Spur Magnetic Anomaly (BSMA) (Bécel et al., 2020; Shuck et al., 2019), which is ∼100–200 km east of the ECMA. The localized, thin crust suggests that a ∼150 km swath of crust between the magnetic anomalies is proto-oceanic and formed during ultraslow spreading. The crust thickens to about 8.5–10 km and attains a smoother topography at the BSMA. This may imply that full sea-floor spreading did not initiate until the emplacement of BSMA (∼170 Ma).

Ambient noise surface waves and long-offset refraction data are primarily sensitive to structure in the crust. The relationship of the lithospheric mantle wavespeed structure and crystalline fabric to crustal structure, magnetic anomalies, and stages of rifting remains unknown. Here, we image the structure of the mantle at the COT. We investigate how the structures are associated with the transition from continental break up to continental spreading and how the lithosphere has subsequently been modified.

1.2. Mantle Flow

Several important geodynamic phenomena have been proposed at ENAM (e.g., Long et al., 2010). Fouch et al. (2000) showed that shear-wave splitting within the continent is consistent with a model where mantle flow is redirected to flow around a deep continental lithospheric keel. Low shear velocity near ENAM could indicate volatile abundance and upwelling material associated with subducted Farallon slab (van der Lee et al., 2008). The strong horizontal temperature gradient in the mantle near the cratonic edge (the keel) can induce edge-driven convection (EDC) (e.g., King & Ritsema, 2000; Ramsay & Pysklywec, 2011; Savage et al., 2017). EDC has been invoked to explain specific seismic velocity features at ENAM (e.g., Savage et al., 2017). Conversely, the slow velocity features may indicate lithospheric delamination and asthenospheric upwelling, which could also account for enigmatic Eocene volcanism (Figure 1; e.g., Biryol et al., 2016; Mazza et al., 2014). Shear-driven upwelling of asthenosphere into a divot in the moving lithosphere has also been suggested to explain mantle anomalies and volcanism (Long et al., 2021). Margin-parallel shear-wave splitting results offshore have been interpreted as reflecting large scale density-driven flow (Lynner & Bodmer, 2017).

Observational constraints on mantle flow at ENAM, particularly beneath the ocean, are limited (e.g., Lynner & Bodmer, 2017; H. Yuan et al., 2011; Yang et al., 2017). Seismic anisotropy is a crucial observational constraint on mantle flow. Our joint velocity/anisotropy tomography model, with sensitivity extending through the asthenosphere, is poised to address mantle flow near the COT of ENAM.

1.3. Anisotropy and Shear-Wave Splitting

Seismic anisotropy measurements can offer insight into patterns of mantle deformation (e.g., Long & Becker, 2010; Silver, 1996; Skemer & Hansen, 2016). Deformation via dislocation creep produces a crystallographic preferred orientation (CPO) due to heterogeneity in the strength of internal slip systems (Karato et al., 2008; Karato & Wu, 1993; Maupin & Park, 2007). Olivine CPO produced in this way is one of the dominant anisotropic signatures associated with mantle flow. Other phenomena can also result in seismic anisotropy, including aligned fractures or melt pockets (e.g., Kendall et al., 2005; Vauchez et al., 2000).

Shear-wave splitting is a common method used to examine seismic anisotropy (Silver & Chan, 1991). Solutions to the Christoffel equation generally give three wave speeds and particle motion polarizations corresponding to a *P* wave and two quasi-*S* waves (Maupin & Park, 2007). Because the quasi-*S* waves travel at different velocities in an anisotropic medium, a time delay between them can accrue. Using the polarization and time delay between the quasi-*S* waves, the strength and orientation of anisotropy can be inferred.

There is a first-order question across the ENAM whether CPO fabrics and anisotropy are dominated by recent processes or record deformation associated with continental collision and breakup. If associated with recent processes, splitting may align with absolute plate motion (APM) or paleo-spreading in the ocean (e.g., Becker et al., 2014; Long et al., 2010; Silver, 1996). APM correlated splitting is observed in the eastern US, but with notable deviations in our study area (Long et al., 2016; Yang et al., 2017). If related to past deformational events, splitting may align with tectonic boundaries (e.g., Long et al., 2010; Silver, 1996). *SK(K)S* phase splitting across the ENAM exhibits a complex pattern of anisotropy that does not fit with either simple explanation. A region of dominantly null and very weak splitting on the continent (Figure 1; Long et al., 2016; Wagner et al., 2012; Yang et al., 2017) might be caused by roughly isotropic material, vertical mantle flow (e.g., Levin et al., 2018), or depth varying anisotropy that effectively cancels. Further, splitting at the OBSs reveals margin-parallel fast-axes (Figure 1; Lynner & Bodmer, 2017). This is neither consistent with paleo-spreading parallel frozen-in anisotropy in the lithosphere nor APM-parallel anisotropy in the sheared asthenosphere (e.g., Becker et al., 2014). Lynner and Bodmer (2017) proposed the splitting is a consequence of modern margin parallel mantle flow. However, splitting of *S(K)KS* phases provides few constraints on the depth of anisotropy in the upper mantle, making it difficult to interpret what geodynamic processes are occurring (e.g., Y. Li et al., 2021; Long et al., 2016; Lynner & Bodmer, 2017; Yang et al., 2017).

In this paper, we provide the first high resolution constraints on 3-D anisotropy and velocity heterogeneity across the COT of the rifted ENAM with sensitivity through the lithosphere-asthenosphere system. We obtained improved anisotropic depth resolution by combining *S*-phase splitting (e.g., Boyd et al., 2004; Hammond & Toomey, 2003) with *S(K)KS* and *PKS* phases in a tomographic method (Eilon et al., 2016). We used a 1500-km-wide seismic array of broadband stations to produce a model that extends from the Appalachians to ~300 km offshore (Figure 1). We interrogate anisotropy that developed during previous tectonic events, and utilize anisotropy to inform modern asthenospheric flow. We utilize isotropic velocity heterogeneity to interrogate the structure of the mantle, which further informs geodynamic processes, as well as to understand the lithospheric-scale structure of the rift and transition from continent to ocean.

2. Methods

We applied a joint velocity and anisotropy tomography method (Eilon et al., 2016). This method uses differential travel times and splitting times of *SK(K)S* and *PKS* phases (collectively called *XKS*) with teleseismic *S* phases to simultaneously solve for 3-D seismic velocity (synonymous with wavespeed) and azimuthal anisotropy. In addition to providing new depth constraints on anisotropic structure, an important strength of this approach is that it addresses the trade-off between anisotropic and isotropic controls on travel times (Bezada et al., 2016; Eilon et al., 2016). The shallower incidence angle of *S*-phases improves depth constraints on anisotropy compared to using *XKS*-phases alone. *S*-phases may accrue splitting outside the study region, and in particular, near their source. Our primary means of addressing source-side splitting is to solve for it tomographically as an event static term (Section S3 in Supporting Information S1; Eilon et al., 2016).

We used broadband data from the ENAM-CSE (up to 1.5 years of data from 30 OBSs and 3 land seismometers), the TA (which was present in the eastern U.S. from 2011 to 2015), and several long-running regional networks for

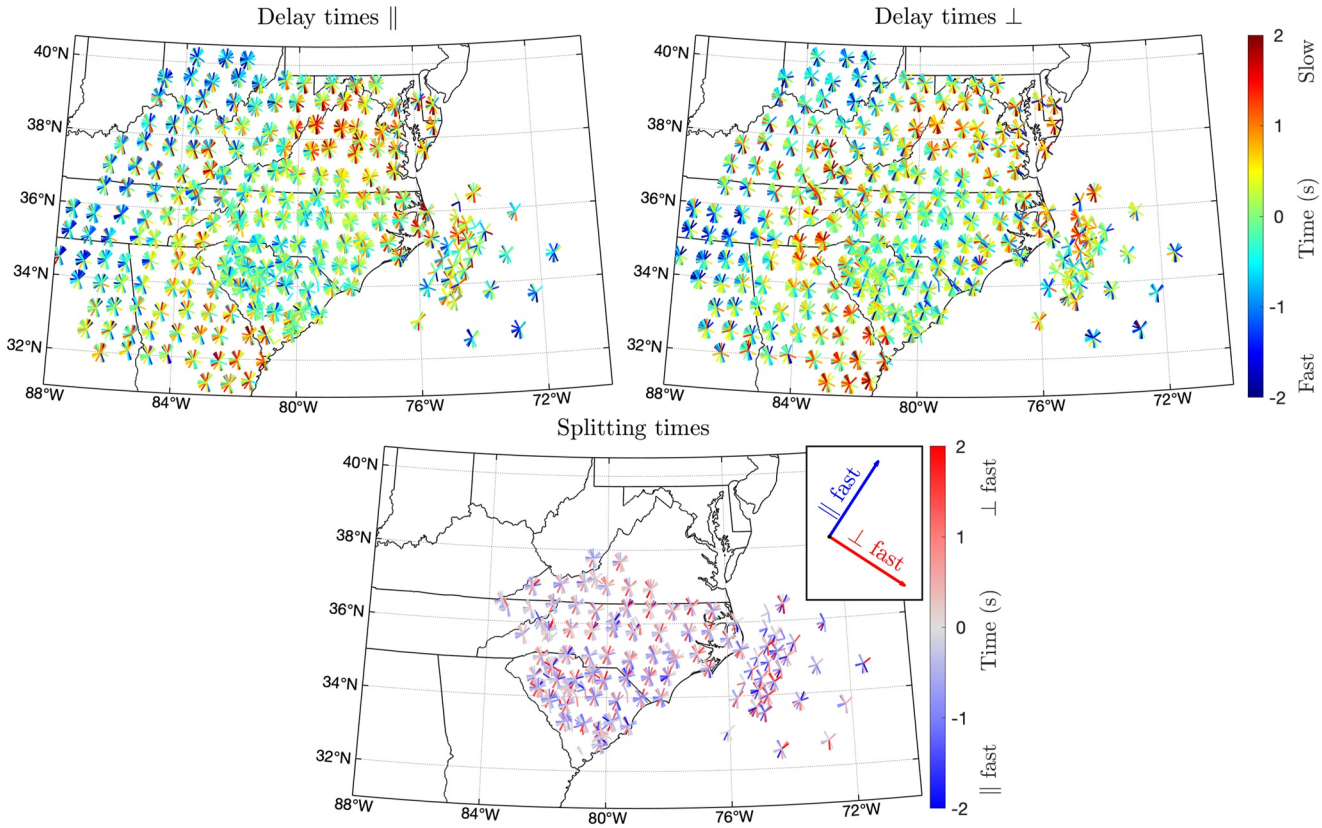

Figure 2. Inverted differential travel times for teleseismic *S*, *S(K)KS*, and *PKS* phases polarized parallel and perpendicular to the symmetry axis, $\delta T_{\parallel}$ and $\delta T_{\perp}$ (top), as well as the measured splitting times, dT_{splt} (bottom). Each measurement is plotted as a line that points toward the earthquake. Note that smaller array bounds are used for measuring splitting to avoid anisotropy with non-constant geometries.

a total of 245 stations (Figure 1). Our earthquake selection criteria (Section S1.1 in Supporting Information S1) leave 2,326 earthquakes which we evaluated from January 2003 to May 2020.

We first measured shear wave splitting times jointly with differential travel times (Section 2.1). We used an augmented multi-channel cross-correlation (MCCC) approach (Eilon et al., 2016). Splitting times were measured as either margin-parallel fast (positive) or margin-perpendicular fast (negative) (Figure 2). Splitting times constrain anisotropy. We jointly measured differential travel times, relative to the arrival times predicted by the IASP91 1-D velocity model (Kennett & Engdahl, 1991), between all stations. The primary role of the differential travel times is to constrain isotropic velocity, although they also inform anisotropy.

Splitting and differential travel times were the input for the tomographic method (Section 2.2; Figures 3–5). We decompose velocities into margin parallel ($V_{\parallel}$) and perpendicular ($V_{\perp}$) components (Figure 4). We jointly inverted these velocities using our splitting and differential travel times (Eilon et al., 2016). Isotropic velocity is simply $(V_{\parallel} + V_{\perp})/2$. Velocity is reported as percent deviation from each layer's average. Differential travel times cannot constrain absolute velocity; by construction, velocity deviations within each layer have an average of zero. Azimuthal anisotropy strength is simply $(V_{\parallel} - V_{\perp})/(V_{\parallel} + V_{\perp})$, so positive values indicate margin-parallel fast and negative values indicate margin-perpendicular fast (Figure 4).

2.1. Anisotropic Multi-Channel Cross-Correlation

To jointly measure splitting and differential travel times, we used the augmented MCCC method of Eilon et al. (2016). This augmented method builds on traditional MCCC (Section S1 in Supporting Information S1; VanDecar & Crosson, 1990). We assume a constant horizontal hexagonal symmetry axis with orientation ϕ = N33°E. This assumption is required to make the tomography math tractable, but also simplifies the splitting measurement method.

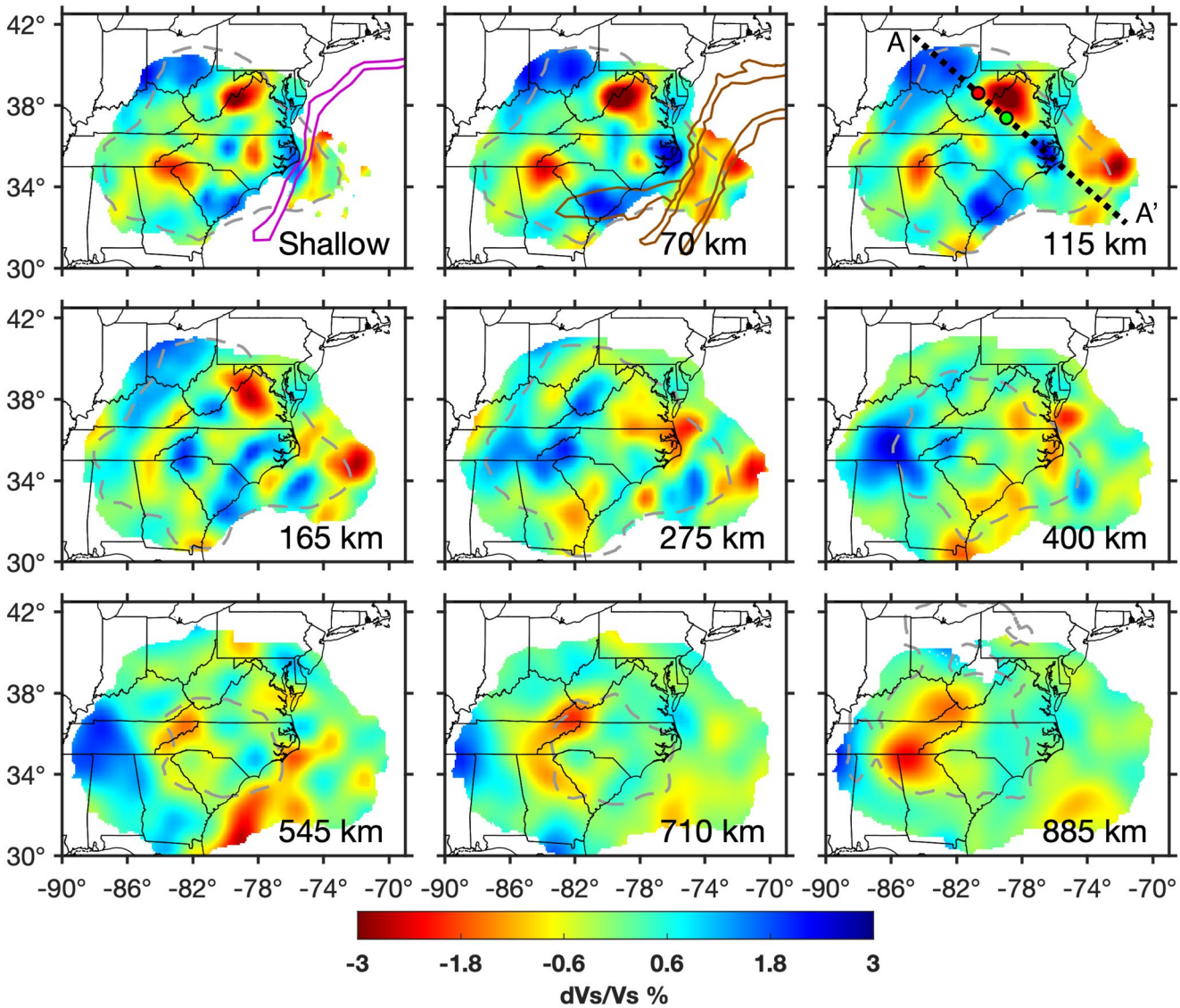

Figure 3. Our isotropic shear velocity model. Each layer shows percent deviation from the layer's average velocity. "Shallow" is our shallowest layer. It contains structure which is too shallow to be vertically resolved and is essentially averaged above ~70 km. Positive Gravity Anomaly (PGA), drawn based on Sandwell and Smith (2009), shown on shallow depth slice as magenta line. Magnetic anomalies, drawn based on Maus et al. (2009), shown on 70 km slice as brown lines. From west to east, they are the BMA, ECMA, and BSMA. Models are only plotted where hit quality exceeds 0.7. The dashed gray contour shows where semblance (a measurement of the similarity between synthetic input and output checkerboard models) exceeds 0.8. Red and green dots on the 115 km slice border the high topography region of the Appalachians. PGA: Positive Gravity Anomaly. BMA: Brunswick Magnetic Anomaly. ECMA: East Coast Magnetic Anomaly. BSMA: Blake Spur Magnetic Anomaly.

The fixed symmetry axis is not equivalent to assuming a fixed fast splitting orientation. Rather, we assume that structure will be organized according to the tectonic geometry: either margin-parallel or margin-perpendicular fast. For most mantle fabrics, the method effectively projects the anisotropic symmetry axis to these directions (Eilon et al., 2016). This anisotropic geometry is chosen on the basis of OBS splitting measurements (which have an average fast polarization of N33°E: Lynner & Bodmer, 2017) as well as splitting measurements in the Appalachians (Figure 1; Long et al., 2016). The assumed anisotropy can produce split quasi-*S* waves polarized approximately parallel and perpendicular to ϕ. These have differential travel times $\delta T_{\parallel}$ and $\delta T_{\perp}$, respectively. The difference between these times at a station is the splitting time dT_{splt}. By incorporating both quasi-*S* waves into MCCC, we simultaneously measured all three delay times. In detail, the relative amplitude of both quasi-*S* waves, and thus the feasibility of measuring splitting, depends on a wave's particle motion polarization (Section S1.2 in Supporting Information S1). For some earthquakes, we can only measure $\delta T_{\parallel}$ or $\delta T_{\perp}$.

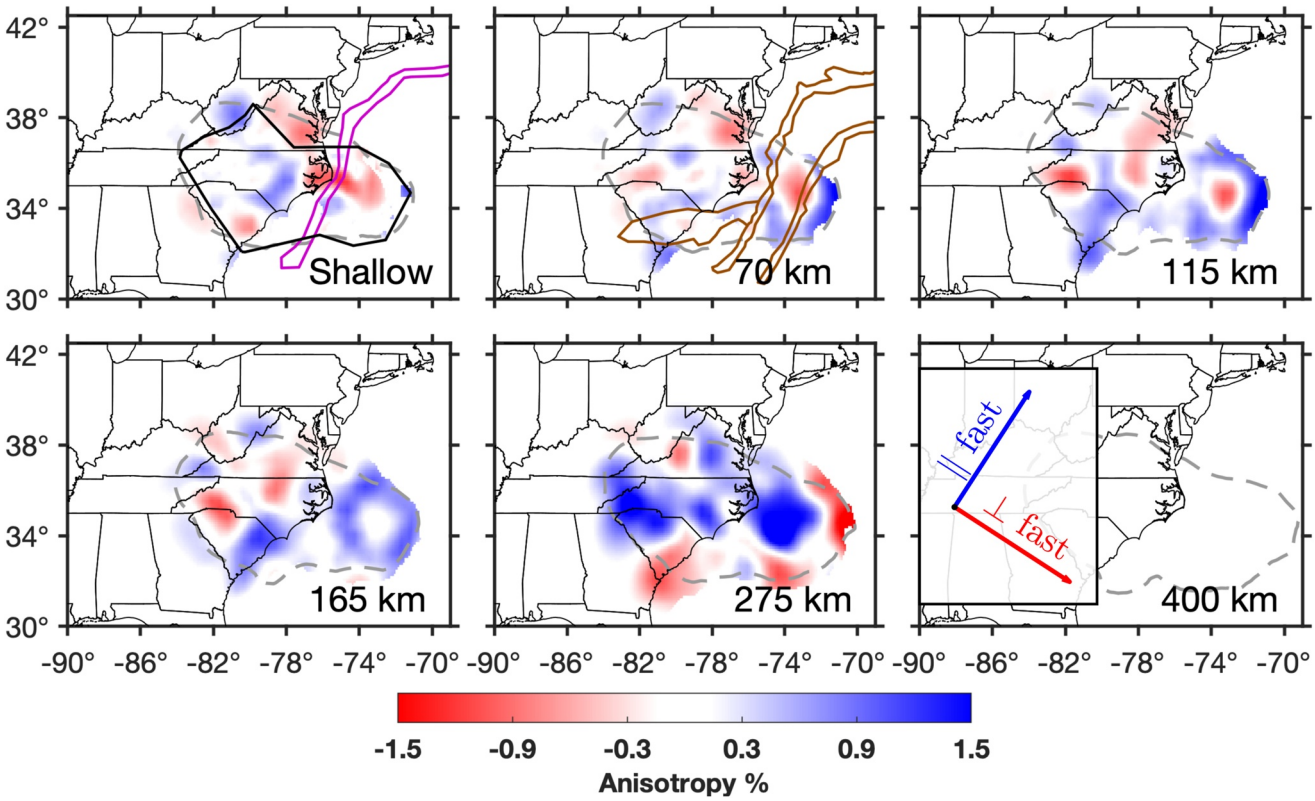

Figure 4. Our anisotropy model. See Figure 3 for description of shallow layer, potential field contours, and masking based on hit quality and semblance. Blue indicates margin-parallel-fast anisotropy and red indicates margin-perpendicular-fast anisotropy. Anisotropy is assumed to be 0 beneath 300 km. The black contour on the "shallow" slice is the region within which we measured splitting times.

The assumed symmetry axis implicitly constrains the geometry of the anisotropic model. We only measure splitting and solve for anisotropy within the area where previous splitting studies show structure consistent with (i.e., mean fast or slow axis <~25° from) our assumed N33°E symmetry (Figure 1 and Figure S1 in Supporting Information S1). Outside this region, we measured differential travel times only and conducted only isotropic tomography, fixing anisotropy to zero (Figures 2 and 4). We preferentially fit splitting data from the stations that best match our assumed symmetry axis. We weighted measurements by $\sqrt{|(45° - \Delta\phi)|/45°}$ where $\Delta\phi$ is the difference between our assumed symmetry axis and the mean fast polarization of literature measurements within the proximity of a station ("splitting misorientation" in Figure S1 in Supporting Information S1). The method might artificially reduce anisotropy where the true symmetry axis deviates from ours, but care taken in choosing where to solve for anisotropy should minimize this.

Our method also assumes that symmetry axes are horizontal, and it is not sensitive to radial anisotropy. Any radial anisotropy will be mapped into our results, but only weakly. This effect is well within the uncertainty of the data (Eilon et al., 2016). Variations in anisotropy orientation with depth could be further problematic. A lack of strong back-azimuthal variability in splitting measurements offers some support that layered anisotropic fabrics are either parallel or perpendicular to each other where we measure splitting times (Yang et al., 2017). Our method is optimal for accounting for such layering. We verified that the complexity of splitting at ENAM is consistent with our simplified anisotropic orientation, supporting that the first order azimuthal anisotropy can be captured by our inversion.

Section S1 in Supporting Information S1 describes quality control and data processing steps used when measuring splitting and travel times, as well as how we incorporated multiple MCCC datasets for different sub-regions (Section S1.1 in Supporting Information S1), along with splitting measurements from the literature (Long et al., 2016; Lynner & Bodmer, 2017; Yang et al., 2017).

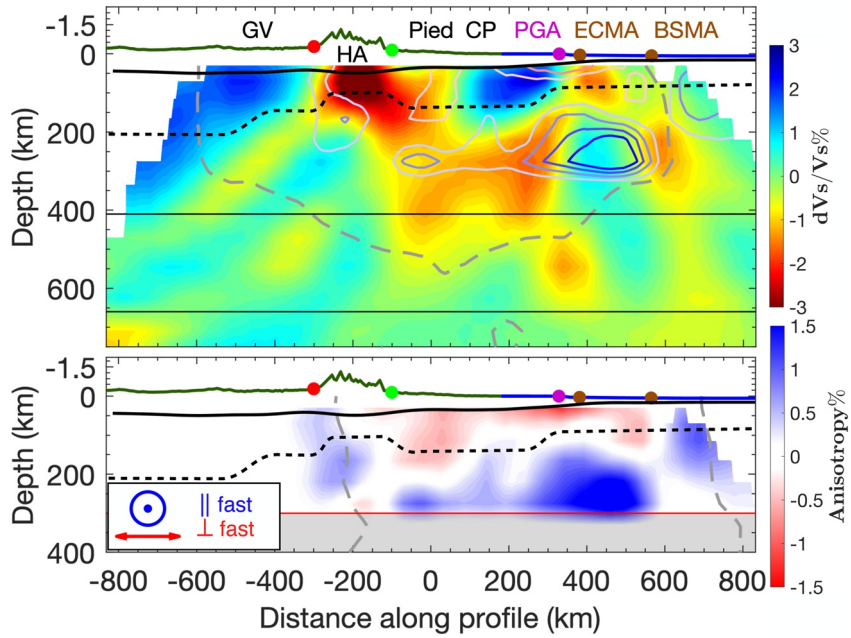

Figure 5. Cross-sections of the velocity (top) and anisotropy (bottom) models. Contours of anisotropy are shown on top of the velocity figure at ±0.4%, 0.75%, 1.1%, and 1.45%. Elevation lines are blue in the ocean and green on land. The red and green dots on the elevation line correspond to the same dots in Figure 3. Mantle transition zone lines are shown at 410 and 660 km. The approximate dislocation creep regime base is indicated as a red line at 300 km depth. We assumed no anisotropy beneath 300 km, which is grayed out. The Moho depth (Shen & Ritzwoller, 2016; Shuck et al., 2019) is shown as a solid black line. We show an approximate, schematic lithosphere-asthenosphere boundary (LAB) as a black, dashed line. Different methods suggest inconsistent LAB depths (e.g., Hopper & Fischer, 2018; Murphy & Egbert, 2019; Pasyanos et al., 2014), so we roughly interpreted the LAB depth based on the high velocity material above ~80–200 km in our model. Cross-sections run from northwest to southeast (A-A' in Figure 3). Only portions of the model where the hit quality is greater than 0.7 is shown. The dashed gray contour shows where semblance (a measurement of the similarity between synthetic input and output checkerboard models) exceeds 0.8. GV: Grenville province. HA: Harrisonburg anomaly. Pied: Piedmont. CP: Coastal plains. PGA: Positive Gravity Anomaly. ECMA: East Coast Magnetic Anomaly. BSMA: Blake Spur Magnetic Anomaly.

2.2. Tomography

We jointly inverted the velocity and anisotropy models using the splitting and differential travel times. It is not feasible to independently resolve the number of parameters required to describe even relatively simple hexagonal anisotropic elasticity. This is largely due to inherent non-linearities and the limits of the data. Instead, we followed the methodology of Eilon et al. (2016) in applying several key assumptions to parsimoniously parameterize the anisotropic elastic tensor (Section S2 in Supporting Information S1). This approach reduces the required parameters at each model node to two: the velocities of shear waves traveling vertically with particle motion polarities parallel ($V_{\parallel}$) and perpendicular ($V_{\perp}$) to the anisotropic symmetry axis. These parameters easily translate to isotropic velocity and anisotropy. Based on simplified formulas for V_{SH} and V_{SV} (Section S2 in Supporting Information S1), we then calculated the differential travel times ($\delta T_{\parallel}$, $\delta T_{\perp}$), and splitting times (dT_{splt}).

We applied *a priori* crustal corrections to account for the influence of known crustal heterogeneity on differential travel times (Section S3 and Figure S2 in Supporting Information S1; e.g., Sandoval et al., 2004). We additionally solved for event and station static terms for splitting and differential travel times (Section S3 in Supporting Information S1). The static terms account for heterogeneity outside the model. We accounted for finite frequency effects using a first Fresnel zone paraxial approximation (Section S4 in Supporting Information S1), which is updated from Schmandt and Humphreys (2010) and Eilon et al. (2015).

The discretization and ray geometry influence where the model is reliably recovered. The model space extends from 30 to 1,080 km depth, with inter-node vertical spacing that increases linearly with depth from 40 to 100 km. Above the depth where rays cross (~70 km), the inversion cannot accurately constrain the depth of heterogeneity. The delay times are still sensitive to structure in this depth range, and structure here will be mapped into station

static terms or the shallow portion of the model. We display the 30 km "shallow structure" layer (Figures 3 and 4) because, although structure here is formally not vertically resolved, this layer still illuminates important lateral heterogeneity. The horizontal span of the model is between latitudes 25°N and 46°N and longitudes 96°W and 63°W. This includes a buffer region beyond the seismic array on all sides, required for well-behaved tomography. We do not interpret or display structure in this buffer region. Horizontal node spacing within the seismometer array is 40 km.

We addressed the mixed-determined tomographic inverse problem using smoothed, damped, least squares (e.g., Menke, 2012). This is equivalent to imposing *a priori* assumptions of relatively simple structure and relatively modest perturbations in velocity and anisotropy. We used "L-tests" to determine the appropriate regularization parameters (Section S5 and Figure S3 in Supporting Information S1).

Anisotropy in the upper mantle is dominantly controlled by the CPO of olivine. This conventionally develops through deformation within the dislocation creep regime. However, with increasing depth, the dominant deformation mechanism of olivine in the mantle transitions from dislocation to diffusion creep (Karato & Wu, 1993). In 1-D Earth reference models, anisotropy (V_{SH}/V_{SV}) tends toward zero by about 300 km depth (Chang et al., 2015). This is much shallower than the base of our model. To prevent erroneous mapping of anisotropy to depths where CPO, and hence anisotropic fabrics, is unlikely, our preferred models assume zero anisotropy beneath 300 km depth. For completeness, we also present models where this assumption is relaxed (Figures S4 and S5 in Supporting Information S1). As expected, in this case, anisotropy extends deeper than the anticipated dislocation creep regime. However, we find that upper mantle features that we interpret remain.

We evaluated how simplifications regarding wave polarization in the forward model (Section S2 in Supporting Information S1) might bias the data fit. We conducted a synthetic splitting test with a more complete parameterization. We propagated Gaussian pulses through our anisotropic model along a given raypath, solving the full Christoffel equation in each layer to find quasi-*S* wave velocities and polarizations. These calculations utilized the back-azimuths and ray parameters from the actual data. In each layer, we sequentially apply splitting to the wavelet. At the top of the model, we measured splitting parameters on the final synthetic waveform using transverse energy minimization, mimicking the processing of real splitting data (Silver & Chan, 1991). Figure S6 in Supporting Information S1 shows one example resulting transverse energy surface. The resulting synthetic fast polarizations closely match observed splitting fast polarizations from the literature over the vast majority of the region (Figure 6).

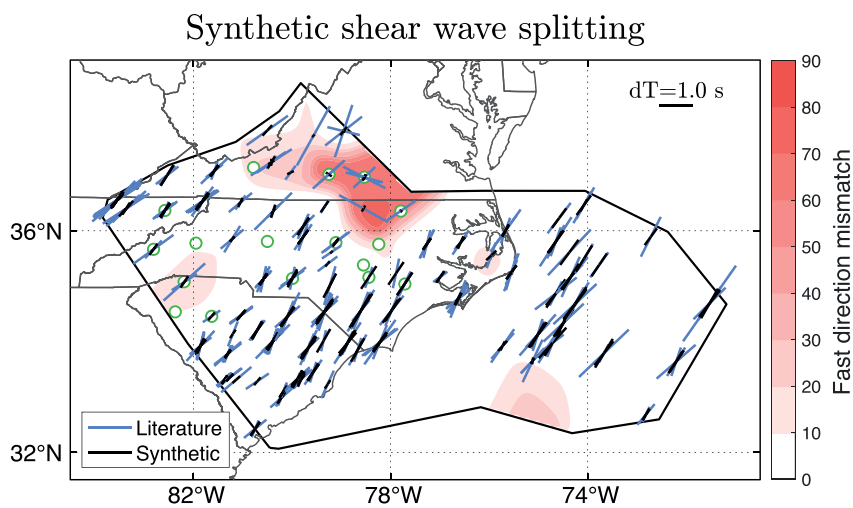

Figure 6. Results of synthetic splitting tests applied to rays for which splitting has been measured in the literature (Long et al., 2016; Lynner & Bodmer, 2017; Yang et al., 2017). We calculated these by first synthetically splitting waveforms and then measuring splitting using transverse energy minimization. This synthetic splitting method is not dependent on the simplifying assumptions regarding waveform polarization from Section 2.2 and Section S2 in Supporting Information S1. The orientations of black and blue lines indicate fast polarizations, and line lengths indicate splitting delay times. Background color indicates the angular misorientation between our synthetic splits and splitting measurements from the literature, which is interpolated to 2-D using a Gaussian filter. Green/white circles indicate stations identified as null splitting stations in Long et al. (2016). We did not apply this analysis where we did not measure splitting, outside the thick black line.

The only notable exception is in the north of our model, where isolated synthetic split fast polarizations approach orthogonal to their literature counterparts. This mismatch is primarily at stations where Long et al. (2016) measured only nulls. Other splitting measurements in the literature become highly variable here, for example rotating from margin parallel to perpendicular across the MAGIC array just north of our study region (Aragon et al., 2017). Our synthetic splitting delay times are small here (<~0.3 s), which is consistent with previous null measurements at those stations, and we place low emphasis on the polarization of the almost null synthetic splits.

3. Results

3.1. Delay Times and Shear Wave Splitting

We used MCCC to measure splitting and differential travel times. The well-aligned and linearized waveforms after undoing the effects of splitting indicate success of the approach (Figure S7 in Supporting Information S1). Weighted variance reduction for differential travel times ($\delta T_{\parallel}$ and $\delta T_{\perp}$) is 66.4%, and for splitting times (dT_{splt}) is 74.3%. On average, particle motion ellipticity for splitting-corrected shear waves is 51% the original ellipticity. We calculated ellipticity as the ratio of eigenvalues in the particle motion covariance matrix (e.g., Silver & Chan, 1991). Of the 2,326 earthquakes, we applied MCCC to 742, yielding 48,428 delay and splitting measurements (Figure 2 and Figure S8 in Supporting Information S1). The remaining earthquakes were rejected based on the quality control criteria (e.g., poor signal-to-noise ratio or poorly aligned waveforms after applying MCCC: Section S1.1 in Supporting Information S1).

We show differential travel times and splitting times both as individual measurements (Figure 2) and as station averages (Figure S8 in Supporting Information S1). Station averaged differential travel times show up to ~1.5 s fast arrivals in the Grenville orogenic belt and up to ~1.3 s slow arrivals at the Harrisonburg anomaly (HA) near the Virginia/West Virginia border (Figure 2 and Figure S8 in Supporting Information S1). The splitting times indicate dominantly margin-parallel-fast splitting offshore (Figure 2 and Figure S8 in Supporting Information S1). On land, they also show dominantly margin-parallel-fast splitting along much of the coastline, most starkly at the North Carolina/South Carolina border (Figure S8 in Supporting Information S1). This is consistent with Long et al. (2016). Different from most previous literature (e.g., Long et al., 2016; Yang et al., 2017), we measured margin-perpendicular splitting over parts of the coastal plains (e.g., in western North Carolina/South Carolina; Figure S8 in Supporting Information S1). However, these measurements are consistent with the transition from margin parallel to perpendicular splitting moving oceanward across the MAGIC seismic array less than ~100 km north of our study region (Aragon et al., 2017). Splitting measurements can often be resolved only if the delay times are fairly large (e.g., at least 0.5 s splitting using periods longer than 8 s in Long et al., 2016). MCCC improves precision over single station measurements (VanDecar & Crosson, 1990), allowing us to identify splitting trends where splitting times are small.

3.2. Resolution

We conducted a suite of resolution tests which are described in Sections S6 and S7 in Supporting Information S1. These include ~2° sized checkerboard tests (Figures S9 and S10 in Supporting Information S1), spike tests (Figures S11 and S12 in Supporting Information S1), and a squeezing test (Figure S13 in Supporting Information S1). These suggest optimal resolution above ~300 km depth, albeit with amplitude reduction of features by ~40%. The anisotropy and velocity models are independently resolved, there is higher resolution onshore than offshore, and the data require that velocity heterogeneity exists to at least 660 km depth. We calculated semblance (the similarity between input and output checkerboard models; e.g., Zelt, 1998), and plot the semblance ≥ 0.8 contour on models (Figures 3–5). Outside of this contour, more caution is required for interpretation.

To understand how specific features of interest might be imaged in our models, we conducted synthetic input-output tests using structures which match different regional predictions (Figures S14 and S15 in Supporting Information S1). Key input velocity features included a fast, thick, Precambrian lithosphere in the northwest of the model and the slow HA (Figure S14 in Supporting Information S1). The main features we interpret, above about 400 km, are all well resolved. A low velocity feature mimicking the HA was recovered with smearing over ~100 km. High velocity anomalies at the COT were recovered well. Two deep anomalies within our models, a high velocity anomaly centered near 500 km depth and a low velocity anomaly centered near 800 km, were

recovered in shape but with only about 30% of their original amplitude. This suggests caution for interpreting mantle transition zone and deeper mantle features, which are not our focus.

The anisotropy input models included two scenarios (Figure S15 in Supporting Information S1). For the offshore region, we tested 1.5% paleo-spreading parallel (margin-perpendicular) fast frozen-in lithospheric anisotropy overlying an equal magnitude margin parallel mantle-flow induced anisotropy. In the continent, we tested a lithospheric layer overlying an asthenospheric layer. This anisotropy could cause previously observed null splitting (Long et al., 2016). Both layers were recovered offshore with ∼50% amplitude loss and a lateral limit to good lithospheric layer recovery about 200 km from the continent. The continental layers were recovered with similar amplitude loss but with better shape preservation. These tests are strong evidence that first order anisotropic mantle structure, including depth variations, should be faithfully imaged by our models. These tests also give evidence that the inversion can distinguish between weak anisotropy and canceling anisotropic fabrics, which both produce small splitting times.

3.3. Tomography Results: Isotropic Velocity Models

The shear velocity models can be seen in Figures 3, 5 and Figure S16 in Supporting Information S1, and 3-D models can be viewed interactively in Figure S18. We also show models inverted without the OBS data, which unsurprisingly lack important offshore features (Figure S17 in Supporting Information S1). A prominent fast velocity structure is observed furthest into the continent above about 200–300 km depth (extending to a maximum depth of ∼400 km). This structure is as much as 2% fast compared to any layer's average. Within the +1% velocity isosurface of this feature, the mean wavespeed is +1.5%. The shallower (<∼200 km depth) portion of this is the cold, thick, continental interior lithosphere (cf. Savage, 2021). However, this feature is near the edge of our array and only its basic structure is clear (Figure S9 in Supporting Information S1). The high velocity lithosphere shallows toward the ocean until it meets the most prominent slow-velocity feature in our model, in Virginia (∼38.5°N, 79°W). This is the previously imaged low-velocity HA (e.g., Long et al., 2021; Savage et al., 2017; Shen & Ritzwoller, 2016; Wagner et al., 2018). This feature dips oceanward from the surface. It is up to ∼5% slow at 70 km depth. The average velocity within the −1% slow isosurface of the HA is −1.9%. Oceanward of the HA, from approximately −100 to 350 km horizontally in Figure 5, we observe a low velocity anomaly just above the 410 km transition zone. This feature appears to connect to the HA.

Several features in the model correspond with magnetic and gravity anomalies. A high velocity feature (up to ∼2% fast at 70 km depth) in southern Georgia closely follows the trend of the Brunswick Magnetic Anomaly (BMA) and South Georgia Rift (SGR) (Figures 1 and 3). Beneath the OBSs, upper mantle velocity tends to be slower than on the continent. The offshore 70 km layer is ∼0%–2% slow compared to the whole layer average. A low velocity band above ∼100 km closely follows the trend of the ECMA and Positive Gravity Anomaly (PGA). This is in the better resolved portion of the offshore region, though resolution of such a fine structure is suspect given our recovery tests (Figure S9 in Supporting Information S1). We also note a low velocity feature, near the edge of the array and thus likely poorly resolved, that correlates with the BSMA (Figure 3). With caution regarding reduced ray coverage offshore, increased delay/splitting noise, and synthetic test results (Figure S9 in Supporting Information S1), we focus our interpretation on only the dominant trends offshore. Some oceanic structures may be artifacts at the edge of our seismic array. For instance, the nearly 3% slow anomaly at 72°W, 35°N, and 165 km depth is likely an artifact (Figure 3 and Figure S16 in Supporting Information S1).

We also observe anomalies deep in the mantle. Checkerboard tests (Figure S9 in Supporting Information S1) suggest not to interpret the low velocity anomalies at 545 km depth offshore of Georgia and Florida. These features are outside the semblance >0.8 contour (Figure 3 and Figure S9 in Supporting Information S1). The <3% fast velocity anomaly that is strongest beneath Tennessee near ∼400 km depth has been previously imaged (e.g., Biryol et al., 2016; Schmandt & Lin, 2014). We do not interpret the strong anomalies beneath about 660 km, which are less well resolved (Figure S9 in Supporting Information S1) and may be a result of using steeply incident *SK(K)S-PKS* rays. Nevertheless, other body wave tomography models similarly show strong anomalies at such depths here (e.g., Golos et al., 2018; Schmandt & Lin, 2014; H. Wang et al., 2019).

3.4. Tomography Results: Anisotropy Models

The anisotropy models can be seen in Figures 4, 5 and Figure S16 in Supporting Information S1, and interactively in Figure S18. As a key result, we observe two layers of anisotropy, both onshore and offshore (Figure 5). Deeper than ~100–150 km offshore, approximately within the asthenosphere, anisotropy is dominantly margin parallel (generally >1% fast). In the offshore lower lithosphere, anisotropy is generally margin-perpendicular/paleo-spreading parallel, up to about 0.8% fast. Our results do not place depth constraint on upper lithospheric anisotropy, and are instead primarily sensitive to the lower lithosphere. The cross-section in Figure 5 runs through the center of the OBSs to give the most reliable sense of offshore anisotropy. However, lithospheric/asthenospheric layering becomes increasingly inconsistent away from the cross-section, where hit quality and resolution decrease (Figure 4). We suggest the model is strong evidence for lithosphere-asthenosphere anisotropic layering.

On the continent, our model shows margin-parallel-fast anisotropy in the asthenosphere (primary trend is >1% fast at 275 km depth) (Figures 4 and 5). This is consistent with dominantly margin parallel splitting from previous work (e.g., Yang et al., 2017). At 165 km depth and above, the model shows some margin-perpendicular anisotropy up to almost 1% fast in the Piedmont and coastal plain (North/South Carolina and Virginia). This is the same region where Long et al. (2016) observed dominantly null splitting. This shallower anisotropy is complex, pocketed with ~100 km wavelength features. Margin-perpendicular-fast anisotropy is consistent with the *Pn* analysis of Buehler and Shearer (2017), which indicates margin-perpendicular-fast anisotropy just beneath the Moho in the coastal plain. This is also consistent with anisotropic surface-wave phase velocities in the low topography region east of the Appalachians, which rotate from margin parallel for periods longer than about 77 s to margin perpendicular for periods between about 77 and 40 s (Wagner et al., 2018). The continental lithosphere has complicated anisotropy, while asthenospheric anisotropy is dominantly margin parallel.

4. Discussion

Our shear velocity and anisotropy models inform hypotheses of rift and drift dynamics, as well as interpretations of present day structures and processes. We first discuss the velocity and anisotropy structures associated with rifting. Second, we discuss the transition from rifting to drifting. Third, we discuss processes and structures which likely occurred and developed during and after the formation of the passive margin. Finally, we discuss the complex relationship between strain and anisotropy. Our observations and interpretations are summarized in Figure 7.

4.1. Rift Structure

Our velocity models show thick Precambrian lithosphere in the northwest, which thins toward the ocean (Figures 3 and 5). At the HA, the lithosphere is greatly thinned. However, the precise depth of the lithosphere-asthenosphere boundary is not easily established using body-wave tomography, which has less sensitivity to variation in velocity with depth than, for example, receiver functions (e.g., L. Liu & Gao, 2018; X. Yuan et al., 2017).

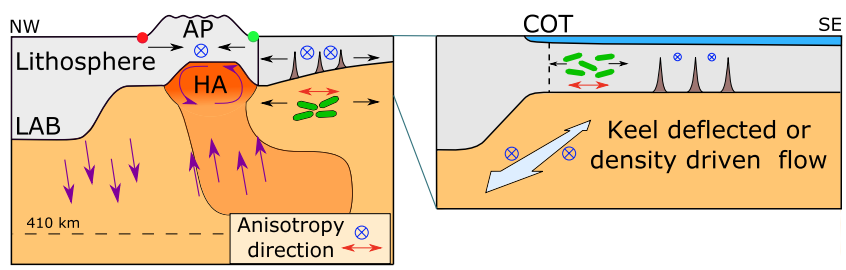

Figure 7. Schematic illustration of the structure and kinematics of ENAM. Red arrows and blue crosses indicate the orientations of anisotropy. Black arrows indicate previous or current extension, compression, or mantle flow. The purple arrows indicate possible edge-driven convection and shear-driven upwelling. Brown dikes are illustrated in the lithosphere. Olivine crystals are illustrated with CPO. Red and green dots correspond to the same regions as in Figures 3 and 5. CPO: Crystallographic-preferred orientation. AP: Appalachian plains. HA: Harrisonburg anomaly. COT: Continent-ocean transition. LAB: Lithosphere-asthenosphere boundary.

Near the SGR, we observe a shallow, high velocity feature, about 2% fast (~81°W, 33°N, 70 km depth) (Figure 3). This distinctly follows the Brunswick positive magnetic anomaly (BMA) and more subtly follows positive gravity anomalies. Wide-angle seismic results suggest that across the failed Georgia rift, high velocity material intruded the lower crust as part of the Central Atlantic Magmatic Province (CAMP) (Marzen et al., 2020). The imaged fast velocity feature is potentially crustal CAMP underplating, with recovery smeared vertically through the lithosphere according to synthetic tests (Figures S9 and S14 in Supporting Information S1). This fast feature extends from the SGR to the COT, and arguably, to some extent, delineates the COT. The connection of the BMA- and SGR-correlated fast velocity anomaly to more fast velocity anomalies delineating the COT suggests that these fast features are of the same cause. Possibly, igneous material from the initial phase of rifting, now solidified, eventually localized from the failed SGR to the COT as part of continental break-up. Alternatively, the fast features near the BMA might be related to an Alleghanian suture (e.g., Hopper et al., 2016; Lizarralde et al., 1994). This fast feature was not clearly resolved in recent mantle tomography models, possibly due to the exclusion of margin-crossing data (e.g., Biryol et al., 2016; Savage, 2021; Wagner et al., 2018).

Our models show laterally complex anisotropy on the continent, above ~200 km depth (Figures 4 and 5). Many rifts exhibit extension-perpendicular (rift-parallel) anisotropy (e.g., Eilon et al., 2014; Kendall et al., 2005; Vauchez et al., 1998, 2000). This is in part due to shape-preferred orientation structures such as dike intrusions and melt lenses. However, if extensional strain and consequent CPO dominates anisotropy, then extension parallel splits should be seen (Tommasi et al., 1999). This is indeed observed in some well-developed rifts (Eilon et al., 2014, 2016) and at mid-ocean ridges (Wolfe & Solomon, 1998). We see a mix of margin parallel anisotropy (i.e., approximately parallel to the Appalachians) and margin perpendicular anisotropy (i.e. approximately parallel to spreading) near the Piedmont and coastal plains (Figures 4 and 5). This is consistent with Aragon et al. (2017). Extension-induced CPO, now frozen in, may explain the lithospheric extension-parallel anisotropy (e.g., Tommasi et al., 1999). Fossil-melt shape-preferred orientation (SPO) may explain some margin parallel anisotropy. However, igneous SPO at rifts is attributed to the strong velocity contrast between melt and host material (e.g., Kendall et al., 2005). This velocity contrast is strongly reduced once melt solidifies. Igneous SPO is a poor candidate for explaining present-day anisotropy, except perhaps near the HA, where melt may be present.

The Appalachians also exhibit convergence-induced anisotropy that is frozen-in (e.g., Long et al., 2016). Splitting is dominantly margin/orogen parallel at the west border of our anisotropic model, where rift deformation is less prominent (Figure 4). The competing influence of convergence, extension, and possibly igneous SPO can produce the complex lithospheric anisotropy we imaged (Figure 4). Such complexity is further expected from laterally heterogeneous volcanism (e.g., Greene et al., 2020) and extension (e.g., Withjack & Schlische, 2005).

Orthogonal and effectively canceling anisotropic layers is one proposed explanation for null splitting in portions of the continental coast (Long et al., 2016; Wagner et al., 2012). We imaged variations in anisotropy with depth, and in particular, the transition to margin parallel in the asthenosphere (Figure 5). Depending on the local magnitudes of anisotropic layers, this is capable of causing null splitting. However, our results cannot rule out the contributions of vertical mantle flow to null splitting measurements because we assumed a horizontal symmetry axis.

4.2. Rift-Drift Transition

4.2.1. Lithospheric Structure

Recent work suggests that proto-oceanic crust was emplaced during the transition from rifting to drifting between the ECMA and BSMA (Bécel et al., 2020; Shuck et al., 2019). We observe a shallow, ~1.5% slow velocity anomaly above ~100 km at the ocean which parallels the ECMA (~74°W, 35°N) (Figure 3). No such feature or trend manifests in the anisotropy model. The gradient in velocity between fast values inboard of the ECMA and slow values seaward of this lineament is suggestive of a relatively rapid contrast in lithospheric thickness (Figures 3, 5, and 7). This is consistent with localized crustal thinning observed by Lynner and Porritt (2017) and C. Li and Gao (2021). We are hesitant to over-interpret small-scale velocity anomalies beneath the ocean in our models. Synthetic tests indicate that resolution here is relatively poor (Figures S9 and S14 in Supporting Information S1). This slow anomaly may reflect persistent continental crust remnant from the rifting process, but that assertion requires further investigation.

There is limited detailed imaging of passive margins at a lithospheric scale to compare our results. In NW Namibia, receiver functions indicate a lithospheric feature that thins from 120 to 80 km at the COT (X. Yuan

et al., 2017). Thinned lithosphere at rifted COTs may be a common theme (Figure 7). Because the African data set is the only other broadband OBS data set to cross a rifted passive margin, our results are some of the first detailed mantle-scale seismic models of a rifted COT.

4.2.2. Preserved Extensional Fabric in Transitional-Oceanic Lithosphere

Globally, anisotropic fast orientations within the oceanic lithosphere tend to align with paleo-spreading (e.g., Becker et al., 2014; Wolfe & Solomon, 1998). This supports the notion that upper mantle anisotropy develops parallel to plate motion and is then frozen within the lithosphere. Although the nearby Cretaceous Atlantic lithosphere shows spreading-parallel fast lithospheric anisotropy (Gaherty et al., 2004), splitting measurements offshore at ENAM are instead margin-parallel-fast (Lynner & Bodmer, 2017). This could corroborate many other studies showing mismatch of anisotropy to paleo-spreading and absolute-plate-motion (APM) (e.g., Dunn et al., 2005; Eilon & Forsyth, 2020; Takeo et al., 2016).

Synthetic tests (Figure S15 in Supporting Information S1) suggest that simple layering is resolved in our models, albeit with reduced amplitudes. We imaged margin parallel anisotropy in the asthenosphere rather than lithosphere (>1% anisotropy beneath ~100 km). The asthenospheric anisotropy produces the surprising offshore splitting measurements (Figure 5). Margin parallel flow can explain the asthenospheric anisotropy (Section 4.3).

We imaged approximately paleo-spreading-parallel anisotropy in the offshore lower lithosphere (Figures 4 and 5). This supports that the oceanic lithosphere preserves CPO of olivine which developed parallel to mid-ocean ridge spreading (e.g., Becker et al., 2014; Russell et al., 2019). We find this layering persists in our model, independent of regularization scheme or whether we assume no anisotropy beneath 300 km (Figures S4 and S5 in Supporting Information S1). Synthetic tests (Figures S10 and S15 in Supporting Information S1) demonstrate that this result is robust, though we only expect to resolve heterogeneity beneath ~70 km. Above this, it is possible that anisotropy rotates to be paleo-spreading perpendicular (e.g., Shuck & Van Avendonk, 2016).

Offshore ENAM, there are only global seismic models for comparison extending beneath the lithosphere. Although global models are highly variable, they tend to show instead margin perpendicular anisotropy in the asthenosphere and have little consensus in the lithosphere (see compilation of Schaeffer et al., 2016). Our models capture the offshore anisotropic layers ultimately absent in global models, demonstrating the importance of utilizing broadband OBSs to accurately characterize the oceans.

4.3. Active Mantle Processes at the Passive Margin

The causes of low velocity anomalies at ENAM, in particular the prominent HA, are subject to debate (e.g., Chu et al., 2013; Mazza et al., 2014). High temperature and possibly partial melt may cause the HA. Savage (2021) estimated up to 2% melt based on the magnitude of their inverted V_s anomaly, and our velocity anomaly is of similar magnitude (about 5% slow). An abrupt increase in attenuation at the HA (Byrnes et al., 2019), high conductivity (Evans et al., 2019), and coincidence with ~48 Ma volcanics (Figure 1; Mazza et al., 2014) also suggests the presence of partial melt. The HA is associated with a dynamic topography anomaly, which likely resulted from buoyant mantle (Ramsay & Pysklywec, 2011; Rowley et al., 2013). Receiver functions indicate thinned lithosphere (Evans et al., 2019). Our models add to a preponderance of evidence that there is a present-day mantle upwelling that significantly perturbs the lithosphere beneath Harrisonburg, VA.

We argue that EDC and shear-driven upwelling are the most likely causes of the HA. Neither of these hypotheses are 100% consistent with all observations, but we argue they match the data better than any alternatives. Although fertile mantle with reduced Mg# can decrease V_s, a reasonable Mg# likely only contributes -1% dV_s (Pollitz & Mooney, 2016). Volatiles, possibly originating from the subducted Farallon slab (van der Lee et al., 2008), could also reduce velocity. However, velocity reduction is likely less than 3% (Pollitz & Mooney, 2016; Savage, 2021), and the anomaly is at least 5% slow in our models. Plume presence (Chu et al., 2013) may not be supported. We see no low velocity plume track connected to the HA in our results and others (Pollitz & Mooney, 2016), and melting temperatures were too cold (Mazza et al., 2014).

EDC is density-driven flow that is excited by strong lateral gradients in temperature at the edge of cold, continental lithosphere (e.g., King, 2007; King & Ritsema, 2000; Shahnas & Pysklywec, 2004). This process may be important at ENAM (e.g., Menke et al., 2016; Ramsay & Pysklywec, 2011). Some have conjectured that the HA represents the low wavespeed, low density upwelling limb of EDC along the margin (e.g., Byrnes et al., 2019;

Savage et al., 2017). Many aspects of our models are consistent with this hypothesis. Despite relative tectonic quiescence in this region, the HA is the slowest feature in the models, suggesting active processes must maintain a velocity contrast. The presence of well established, high velocity lithosphere beginning ~400 km northwest from this feature is consistent with a cold, thick lithospheric edge where the downwelling limbs of convective cells could originate (Figure 5). The eastward dipping low velocity anomaly that is connected to the HA (see also models of Wagner et al., 2018), which extends to the 410 km mantle transition zone (Figure 5), may be the warm, upwelling limb of the convective cell. Unfortunately, anisotropic coverage in our model is limited where we interpret EDC. However, we do not detect strong azimuthal anisotropy at the HA (Figure 5). This is (non-uniquely) consistent with a complex EDC upwelling (e.g., Long et al., 2010). These structures match the geodynamic setting for EDC (e.g., King & Anderson, 1998).

Not all aspects of our model are straightforwardly consistent with EDC. First, we do not see a high velocity downwelling (Figure 5). Second, shear-wave splitting does not approach null above the HA (Aragon et al., 2017), and there is no radial splitting pattern surrounding the HA (e.g., Yang et al., 2017). In ideal conditions, a mantle upwelling might produce these patterns (e.g., Levin et al., 2018). Lastly, the model shows margin parallel anisotropy coincident with this dipping feature (Figure 5), which is difficult to reconcile with a mantle upwelling model. EDC is viable, despite these caveats. The downwelling material may not be easily detectable seismically, and the complex geodynamic setting might promote complicated EDC geometry (e.g., Duvernay et al., 2021; D. Liu & Chen, 2019). We note that a high seismic velocity anomaly has been imaged dipping from the lithosphere at least to the mantle transition zone at the west edge of our model (e.g., Biryol et al., 2016; Schmandt & Lin, 2014), which could be a downwelling. The low velocity material that dips oceanward from the HA (Figures 5 and 7) suggests that upwelling that is not purely vertical, explaining the lack of radial or null splitting above the HA. The combination of HA upwelling, margin parallel flow processes (Section 4.3.1), and APM induced anisotropy likely precludes a straightforward comparison with any idealized mantle flow model.

EDC upwellings can occur in laterally isolated cells (Ramsay & Pysklywec, 2011). Our model shows similar, lower amplitude anomalies elsewhere along the margin (Figure 3). The presence of a low velocity anomaly just above the 410 km mantle transition zone, southeast of the HA (Figure 5), may further be associated with EDC. This could result from a convection cell or upwelling feature between the COT and the HA. Some 3-D EDC models might predict similar features (Kaislaniemi & Van Hunen, 2014). Modeling of the analogous African margin (Kaislaniemi & Van Hunen, 2014) also suggests a margin-parallel component of flow is possible with EDC. This could explain some disconnect between the expected margin perpendicular convective flow and anisotropy. The EDC-like low-velocity anomalies imaged here are in addition to the low velocity Georgia anomaly (only peripherally imaged here: Biryol et al., 2016), a low velocity mantle anomaly in Texas (Pollitz & Mooney, 2016), and the Northern Appalachian Anomaly (Menke et al., 2016). Such variations in EDC along strike are expected based on some modeling, rather than a 2.5-D convective cell (e.g., Ramsay & Pysklywec, 2011). EDC is an attractive hypothesis for explaining a variety of discontinuous, short-wavelength, upper mantle velocity features imaged here and elsewhere without invoking multiple processes (Menke et al., 2016).

Another appealing explanation of the HA is shear-driven upwelling (e.g., Long et al., 2021). This is highly localized asthenospheric upwelling caused by lithospheric motion in the case that the LAB has concave-down divots (Figure 7; Conrad et al., 2010). This hypothesis would not require a downwelling, cold, high seismic velocity limb. Additionally, such upwelling may not erase azimuthal anisotropy due to its dip and short vertical extent (Conrad et al., 2010), so it is broadly consistent with previous splitting results. However, shear-driven upwelling does not predict upwelling or partial melt extending several hundred km beneath the lithosphere (e.g., Conrad et al., 2010), leaving the oceanward dipping, low velocity anomaly unexplained (Figure 5). It is also possible that widespread EDC could be locally compounded by shear-driven upwelling (Duvernay et al., 2021), creating the distinctly seismically slow HA.

Another frequently invoked geodynamic process beneath ENAM is delamination of the lithosphere. In this scenario, the HA results from asthenospheric return flow (e.g., Biryol et al., 2016; Byrnes et al., 2019; Mazza et al., 2014). Previous delamination, or plume erosion, may have carved the lithospheric gap and promoted shear-driven upwelling, or possibly EDC (e.g., Byrnes et al., 2019; Tao et al., 2021).

The craton keel might redirect horizontally flowing mantle around the continent, producing keel-parallel flow. Some splitting trends in the continent have been attributed to this phenomenon (e.g., Fouch et al., 2000; Yang

et al., 2017). Our model shows margin parallel asthenospheric anisotropy well within the continent (Figure 5), consistent with keel-deflected flow.

APM has a first order influence on anisotropy over much of the eastern US, though this correlation is reduced in our study area (e.g., Lynner & Bodmer, 2017; Yang et al., 2017). Where other mantle processes are vigorous, the APM fabric is disrupted or overwhelmed (e.g., Levin et al., 2018). We infer margin parallel mantle flow (Section 4.3.1) in conjunction with small-scale convection, which explains the local deviation in splitting measurements from APM.

4.3.1. Offshore Asthenospheric Flow and Anisotropy

Density-driven flow may also contribute to margin parallel anisotropy offshore ENAM (Lynner & Bodmer, 2017). Globally, asthenospheric anisotropy beneath the oceans tends to align with plate motion, with maximum match at ~200 km depth (Becker et al., 2014). Limited data makes this trend difficult to assess at rifted continent-ocean transitions. In the asthenosphere, our model surprisingly shows anisotropy perpendicular to current plate motion and paleo-spreading (Figures 1 and 5).

Plate motion has only a partial control on asthenospheric shear, and inclusion of density-driven flow is needed to explain anisotropy in much of the oceanic asthenosphere (Becker et al., 2014). Density driven flow could help explain oceanic margin-parallel anisotropy seen in the deeper layers of our models (Lynner & Bodmer, 2017). The two layer lithosphere-asthenosphere mantle flow model of W. Wang and Becker (2019) predicted roughly margin-perpendicular splitting offshore. By adding 3-D flow driven by density anomalies, splitting becomes more margin parallel (W. Wang & Becker, 2019). Some other density-driven mantle flow models also show approximately margin parallel flow here (e.g., Rowley et al., 2013).

The asthenosphere may flow parallel to the margin, around the continental keel, or around a lithospheric step at the COT (Section 4.3; e.g., Fouch et al., 2000). If it is possible for keel deflection to affect the region at least 200–400 km offshore, it might explain the margin-parallel, asthenospheric anisotropy (Figure 5). For the geodynamic model of W. Wang and Becker (2019), when a COT lithospheric step is added with a low viscocity oceanic asthenosphere, the predicted splitting fast orientations become much more closely aligned to the measured fast orientations offshore.

4.4. Relationship Between Anisotropic Fabric and Strain

The fast polarization of splitting is usually assumed to indicate modern mantle deformation (e.g., Zhang & Karato, 1995). However, recent experiments have revealed several complexities in mantle CPO development (e.g., Skemer & Hansen, 2016) that require consideration of time-integrated strain patterns (Kaminski & Ribe, 2002). For example, static annealing can modify otherwise steady CPO through time (Boneh et al., 2017). Our model does show some paleo-spreading perpendicular anisotropy in the offshore lithosphere (Figure 4), albeit where resolution is reduced (Figure S9 in Supporting Information S1). Since this is nearly 200 ma lithosphere, static annealing may partially account for reoriented CPO.

If CPO is already present, then overprinting fabrics to reflect changed asthenospheric flow can require substantial strain, sometimes up to several hundred percent (Boneh et al., 2015; Boneh & Skemer, 2014; Skemer et al., 2012). For small strain, CPO may be in a transient state and not reflect modern asthenospheric flow in a simple way. CPO may similarly be in a transient state if asthenospheric flow orientation changes over small spatial and temporal scales (Kaminski & Ribe, 2002; Skemer et al., 2012). Anisotropy may not clearly reflect asthenospheric flow in convective systems spanning short distances, or where mantle flow changes through time, such as EDC (e.g. Kaislaniemi & Van Hunen, 2014). In the asthenosphere, our anisotropy model shows some heterogeneity at wavelengths down to ~100 km (Figure 4). We speculate that flow at this scale might have produced transient state anisotropy with fast orientations not clearly reflecting modern mantle flow. Northwest of the HA, within the asthenosphere, we predict margin-perpendicular EDC to produce margin-perpendicular anisotropy. However, we observe complicated, yet more dominantly margin parallel, anisotropy. This may be a result of transient-state CPO. In contrast, for larger-scale margin parallel asthenospheric flow, particularly beneath the ocean, CPO should reach steady state and produce margin parallel anisotropy. This matches the more strongly margin-parallel asthenospheric anisotropy offshore (Figures 4 and 5).

5. Conclusion

We present *S*-wave tomography models from a passive broadband data set spanning the COT of the ENAM. Our inversion technique places depth constraints on isotropic and anisotropic structures. It also resolves trade-offs present in single-parameter inversions by simultaneous fitting of travel time and shear wave splitting data. The resultant models provide the first high-resolution images of seismic velocity and azimuthal anisotropy to sub-lithospheric depth across the COT.

Offshore, we find that the rifted continental to oceanic lower lithosphere preserves extension-parallel anisotropy. Onshore, complex lithospheric anisotropy likely reflects the competing effects of extension and convergence over several Wilson cycles. In the asthenosphere, margin parallel anisotropy dominates. This may reflect mantle flow due to density gradients or pressure gradients and may be associated with a step in lithospheric thickness. Isotropic velocities within the continent show the thick, high-velocity continental keel inboard of the Appalachians and the low-velocity Harrisonburg anomaly associated with Eocene volcanics. This latter feature, together with other small-wavelength velocity anomalies, are roughly consistent with edge-driven convection, possibly in tandem with shear driven upwelling, revealing that active mantle flow processes have strong influence at the passive margin.

These results, made possible by an unusual amphibious broadband data set, demonstrate the dynamic and complex nature of mantle processes at the rifted COT. This study, together with other products of the ENAM-CSE, reinforces the importance of shoreline-crossing instrumentation.

Data Availability Statement

Shear-wave splitting from previous literature is available as published Supporting Information S1 (Long et al., 2016; Lynner & Bodmer, 2017; Yang et al., 2017). All waveform data is available through the IRIS Data Management Center (Suárez et al., 2008). We used network codes TA (IRIS Transportable Array, 2003), YO (Gaherty, 2014), CO (University of South Carolina, 1987), ET (University of Memphis, 1982), N4 (Albuquerque Seismological Laboratory (ASL)/USGS, 2013), PE (Penn State University, 2004), SP (University of South Carolina, 2000), SS (Single Station), XQ (Wagner, 2012), and Z4 (Wagner, 2009).

Acknowledgments
We thank Toshiro Tanimoto and Robin Matoza for suggestions which improved the manuscript. We thank Stephen S. Gao and an anonymous reviewer for insightful comments that improved the manuscript. This work was funded by NSF OCE 1753722 and OCE 2001145.

References

Abt, D. L., Fischer, K. M., French, S. W., Ford, H. A., Yuan, H., & Romanowicz, B. (2010). North American lithospheric discontinuity structure imaged by Ps and Sp receiver functions. *Journal of Geophysical Research*, *115*(B9), B09301. https://doi.org/10.1029/2009JB006914

Akintunde, O. M., Knapp, C. C., & Knapp, J. H. (2014). Tectonic significance of porosity and permeability regimes in the red beds formations of the South Georgia Rift Basin. *Tectonophysics*, *632*, 1–7. https://doi.org/10.1016/j.tecto.2014.07.029

Albuquerque Seismological Laboratory (ASL)/USGS. (2013). *Central and Eastern US Network [Data set]*. International Federation of Digital Seismograph Networks. https://doi.org/10.7914/SN/N4

Aragon, J. C., Long, M. D., & Benoit, M. H. (2017). Lateral variations in SKS splitting across the MAGIC array, central Appalachians. *Geochemistry, Geophysics, Geosystems*, *18*(11), 4136–4155. https://doi.org/10.1002/2017GC007169

Bécel, A., Davis, J. K., Shuck, B. D., Van Avendonk, H. J. A., & Gibson, J. C. (2020). Evidence for a prolonged continental breakup resulting from slow extension rates at the eastern North American volcanic rifted margin. *Journal of Geophysical Research: Solid Earth*, *125*(9), 1–27. https://doi.org/10.1029/2020JB020093

Becker, T. W., Conrad, C. P., Schaeffer, A. J., & Lebedev, S. (2014). Origin of azimuthal seismic anisotropy in oceanic plates and mantle. *Earth and Planetary Science Letters*, *401*(1), 236–250. https://doi.org/10.1016/j.epsl.2014.06.014

Bedle, H., & van der Lee, S. (2009). S velocity variations beneath North America. *Journal of Geophysical Research*, *114*(B7), 1–22. https://doi.org/10.1029/2008JB005949

Begg, G., Griffin, W., Natapov, L., O'Reilly, S. Y., Grand, S., O'Neill, C., et al. (2009). The lithospheric architecture of Africa: Seismic tomography, mantle petrology, and tectonic evolution. *Geosphere*, *5*(1), 23–50. https://doi.org/10.1130/GES00179.1

Bezada, M. J., Faccenda, M., & Toomey, D. R. (2016). Representing anisotropic subduction zones with isotropic velocity models: A characterization of the problem and some steps on a possible path forward. *Geochemistry, Geophysics, Geosystems*, *17*(8), 3164–3189. https://doi.org/10.1002/2016GC006507

Biryol, C. B., Wagner, L. S., Fischer, K. M., & Hawman, R. B. (2016). Relationship between observed upper mantle structures and recent tectonic activity across the Southeastern United States. *Journal of Geophysical Research: Solid Earth*, *121*(5), 3393–3414. https://doi.org/10.1002/2015JB012698

Boneh, Y., Morales, L. F., Kaminski, E., & Skemer, P. (2015). Modeling olivine CPO evolution with complex deformation histories: Implications for the interpretation of seismic anisotropy in the mantle. *Geochemistry, Geophysics, Geosystems*, *16*(10), 3436–3455. https://doi.org/10.1002/2015GC005964

Boneh, Y., & Skemer, P. (2014). The effect of deformation history on the evolution of olivine CPO. *Earth and Planetary Science Letters*, *406*, 213–222. https://doi.org/10.1016/j.epsl.2014.09.018

Boneh, Y., Wallis, D., Hansen, L. N., Krawczynski, M. J., & Skemer, P. (2017). Oriented grain growth and modification of 'frozen anisotropy' in the lithospheric mantle. *Earth and Planetary Science Letters*, *474*, 368–374. https://doi.org/10.1016/j.epsl.2017.06.050

Boyd, O. S., Jones, C. H., & Sheehan, A. F. (2004). Foundering lithosphere imaged beneath the southern Sierra Nevada, California, USA. *Science*, *305*(5684), 660–662. https://doi.org/10.1126/science.1099181

Buehler, J. S., & Shearer, P. M. (2017). Uppermost mantle seismic velocity structure beneath USArray. *Journal of Geophysical Research: Solid Earth*, *122*(1), 436–448. https://doi.org/10.1002/2016JB013265

Byrnes, J. S., Bezada, M., Long, M. D., & Benoit, M. H. (2019). Thin lithosphere beneath the central Appalachian Mountains: Constraints from seismic attenuation beneath the MAGIC array. *Earth and Planetary Science Letters*, *519*(1), 297–307. https://doi.org/10.1016/j.epsl.2019.04.045

Chang, S., Ferreira, A. M. G., Ritsema, J., van Heijst, H. J., & Woodhouse, J. H. (2015). Joint inversion for global isotropic and radially anisotropic mantle structure including crustal thickness perturbations. *Journal of Geophysical Research: Solid Earth*, *120*(6), 4278–4300. https://doi.org/10.1002/2014JB011824

Chowns, T. M., & Williams, C. T. (1983). *Pre-Cretaceous rocks beneath the Georgia coastal plain—Regional implications*. US Geological Survey Professional Paper, 1313-A, 1–42. https://doi.org/10.3133/pp1313

Chu, R., Leng, W., Helmberger, D. V., & Gurnis, M. (2013). Hidden hotspot track beneath the eastern United States. *Nature Geoscience*, *6*, 963–966. https://doi.org/10.1038/ngeo1949

Conrad, C. P., Wu, B., Smith, E. I., Bianco, T. A., & Tibbetts, A. (2010). Shear-driven upwelling induced by lateral viscosity variations and asthenospheric shear: A mechanism for intraplate volcanism. *Physics of the Earth and Planetary Interiors*, *178*(3–4), 162–175. https://doi.org/10.1016/j.pepi.2009.10.001

Crosby, A., White, N., Edwards, G., & Shillington, D. J. (2008). Evolution of the Newfoundland–Iberia conjugate rifted margins. *Earth and Planetary Science Letters*, *273*(1–2), 214–226. https://doi.org/10.1016/j.epsl.2008.06.039

DeMets, C., Gordon, R. G., & Argus, D. F. (2010). Geologically current plate motions. *Geophysical Journal International*, *181*(1), 1–80. https://doi.org/10.1111/j.1365-246X.2009.04491.x

Dunn, R. A., Lekić, V., Detrick, R. S., & Toomey, D. R. (2005). Three-dimensional seismic structure of the Mid-Atlantic Ridge (35N): Evidence for focused melt supply and lower crustal dike injection. *Journal of Geophysical Research*, *110*(B9), 1–17. https://doi.org/10.1029/2004JB003473

Duvernay, T., Davies, D. R., Mathews, C. R., Gibson, A. H., & Kramer, S. C. (2021). Linking intraplate volcanism to lithospheric structure and asthenospheric flow. *Geochemistry, Geophysics, Geosystems*, *22*(8), e2021GC009953. https://doi.org/10.1029/2021GC009953

Eilon, Z., Abers, G. A., & Gaherty, J. B. (2016). A joint inversion for shear velocity and anisotropy: The Woodlark Rift, Papua New Guinea. *Geophysical Journal International*, *206*(2), 807–824. https://doi.org/10.1093/gji/ggw177

Eilon, Z., Abers, G. A., Gaherty, J. B., & Jin, G. (2015). Imaging continental breakup using teleseismic body waves: The Woodlark Rift, Papua New Guinea. *Geochemistry, Geophysics, Geosystems*, *16*(8), 2529–2548. https://doi.org/10.1002/2015GC005835

Eilon, Z., Abers, G. A., Jin, G., & Gaherty, J. B. (2014). Anisotropy beneath a highly extended continental rift. *Geochemistry, Geophysics, Geosystems*, *15*(3), 545–564. https://doi.org/10.1002/2013GC005092

Eilon, Z. C., & Forsyth, D. W. (2020). Depth-dependent azimuthal anisotropy beneath the Juan de Fuca Plate system. *Journal of Geophysical Research: Solid Earth*, *125*(8), 1–17. https://doi.org/10.1029/2020JB019477

Evans, R. L., Benoit, M. H., Long, M. D., Elsenbeck, J., Ford, H. A., Zhu, J., & Garcia, X. (2019). Thin lithosphere beneath the central Appalachian Mountains: A combined seismic and magnetotelluric study. *Earth and Planetary Science Letters*, *519*(1), 308–316. https://doi.org/10.1016/j.epsl.2019.04.046

Forte, A. M., Mitrovica, J. X., Moucha, R., Simmons, N. A., & Grand, S. P. (2007). Descent of the ancient Farallon slab drives localized mantle flow below the New Madrid seismic zone. *Geophysical Research Letters*, *34*(4), 1–5. https://doi.org/10.1029/2006GL027895

Fouch, M. J., Fischer, K. M., Parmentier, E. M., Wysession, M. E., & Clarke, T. J. (2000). Shear wave splitting, continental keels, and patterns of mantle flow. *Journal of Geophysical Research*, *105*(B3), 6255–6275. https://doi.org/10.1029/1999JB900372

Gaherty, J. (2014). *Eastern North American Margin Community Seismic Experiment* [Data set]. International Federation of Digital Seismograph Networks. https://doi.org/10.7914/SN/YO_2014

Gaherty, J. B., Lizarralde, D., Collins, J. A., Hirth, G., & Kim, S. (2004). Mantle deformation during slow seafloor spreading constrained by observations of seismic anisotropy in the western Atlantic. *Earth and Planetary Science Letters*, *228*(3–4), 255–265. https://doi.org/10.1016/j.epsl.2004.10.026

Golos, E. M., Fang, H., Yao, H., Zhang, H., Burdick, S., Vernon, F., et al. (2018). Shear wave tomography beneath the United States using a joint inversion of surface and body waves. *Journal of Geophysical Research: Solid Earth*, *123*(6), 5169–5189. https://doi.org/10.1029/2017JB014894

Greene, J. A., Tominaga, M., & Miller, N. C. (2020). Along-margin variations in breakup volcanism at the eastern North American margin. *Journal of Geophysical Research: Solid Earth*, *125*(12), 1–22. https://doi.org/10.1029/2020JB020040

Gripp, A. E., & Gordon, R. G. (2002). Young tracks of hotspots and current plate velocities. *Geophysical Journal International*, *150*(2), 321–361. https://doi.org/10.1046/j.1365-246X.2002.01627.x

Guo, W., Zhao, S., Wang, F., Yang, Z., Jia, S., & Liu, Z. (2019). Crustal structure of the eastern Piedmont and Atlantic coastal plain in North Carolina and Virginia, eastern North American margin. *Earth, Planets and Space*, *71*, 69. https://doi.org/10.1186/s40623-019-1049-z

Hammond, W. C., & Toomey, D. R. (2003). Seismic velocity anisotropy and heterogeneity beneath the Mantle Electromagnetic and Tomography Experiment (MELT) region of the East Pacific Rise from analysis of P and S body waves. *Journal of Geophysical Research*, *108*(B4), 2176. https://doi.org/10.1029/2002JB001789

Hess, H. H. (1962). History of ocean basins. In *Petrologic studies* (pp. 599–620). Geological Society of America. https://doi.org/10.1130/Petrologic.1962.599

Hopper, E., & Fischer, K. M. (2018). The changing face of the lithosphere-asthenosphere boundary: Imaging continental scale patterns in upper mantle structure across the contiguous U.S. with Sp converted waves. *Geochemistry, Geophysics, Geosystems*, *19*(8), 2593–2614. https://doi.org/10.1029/2018GC007476

Hopper, E., Fischer, K. M., Rondenay, S., Hawman, R. B., & Wagner, L. S. (2016). Imaging crustal structure beneath the southern Appalachians with wavefield migration. *Geophysical Research Letters*, *43*(23), 12054–12062. https://doi.org/10.1002/2016GL071005

Huismans, R., & Beaumont, C. (2011). Depth-dependent extension, two-stage breakup and cratonic underplating at rifted margins. *Nature*, *473*, 74–78. https://doi.org/10.1038/nature09988

IRIS Transportable Array. (2003). *USArray Transportable Array [Data set]*. International Federation of Digital Seismograph Networks. https://doi.org/10.7914/SN/TA

Kaislaniemi, L., & Van Hunen, J. (2014). Dynamics of lithospheric thinning and mantle melting by edge-driven convection: Application to Moroccan Atlas Mountains. *Geochemistry, Geophysics, Geosystems*, *15*(8), 3175–3189. https://doi.org/10.1002/2014GC005414

Kaminski, É., & Ribe, N. M. (2002). Timescales for the evolution of seismic anisotropy in mantle flow. *Geochemistry, Geophysics, Geosystems*, *3*(1), 1–17. https://doi.org/10.1029/2001GC000222

Karato, S.-I., Jung, H., Katayama, I., & Skemer, P. (2008). Geodynamic significance of seismic anisotropy of the upper mantle: New insights from laboratory studies. *Annual Review of Earth and Planetary Sciences*, *36*, 59–95. https://doi.org/10.1146/annurev.earth.36.031207.124120

Karato, S.-I., & Wu, P. (1993). Rheology of the upper mantle: A synthesis. *Science*, *260*(5109), 771–778. https://doi.org/10.1126/science.260.5109.771

Kendall, J.-M., Stuart, G. W., Ebinger, C. J., Bastow, I. D., & Keir, D. (2005). Magma-assisted rifting in Ethiopia. *Nature*, *433*, 146–148. https://doi.org/10.1038/nature03161

Kennett, B. L. N., & Engdahl, E. R. (1991). Traveltimes for global earthquake location and phase identification. *Geophysical Journal International*, *105*(2), 429–465. https://doi.org/10.1111/j.1365-246X.1991.tb06724.x

King, S. D. (2007). Hotspots and edge-driven convection. *Geology*, *35*(3), 223–226. https://doi.org/10.1130/G23291A.1

King, S. D., & Anderson, D. L. (1998). Edge-driven convection. *Earth and Planetary Science Letters*, *160*(3–4), 289–296. https://doi.org/10.1016/S0012-821X(98)00089-2

King, S. D., & Ritsema, J. (2000). African hot spot volcanism: Small-scale convection in the upper mantle beneath cratons. *Science*, *290*(5494), 1137–1140. https://doi.org/10.1126/science.290.5494.1137

Larsen, H. C., Mohn, G., Nirrengarten, M., Sun, Z., Stock, J., Jian, Z., et al. (2018). Rapid transition from continental breakup to igneous oceanic crust in the South China Sea. *Nature Geoscience*, *11*, 782–789. https://doi.org/10.1038/s41561-018-0198-1

Levin, V., Long, M. D., Skryzalin, P., Li, Y., & López, I. (2018). Seismic evidence for a recently formed mantle upwelling beneath New England. *Geology*, *46*(1), 87–90. https://doi.org/10.1130/G39641.1

Li, C., & Gao, H. (2021). Modification of crust and mantle lithosphere beneath the southern part of the eastern North American passive margin. *Geophysical Research Letters*, *48*(16), e2020GL090555. https://doi.org/10.1029/2020GL090555

Li, Y., Levin, V., Nikulin, A., & Chen, X. (2021). Systematic mapping of upper mantle seismic discontinuities beneath northeastern North America. *Geochemistry, Geophysics, Geosystems*, *22*(7), e2021GC009710. https://doi.org/10.1029/2021GC009710

Liu, D., & Chen, L. (2019). Edge-driven convection and thinning of craton lithosphere: Two-dimensional thermal-mechanical modeling. *Science China Earth Sciences*, *62*, 2106–2120. https://doi.org/10.1007/s11430-019-9371-0

Liu, L., & Gao, S. S. (2018). Lithospheric layering beneath the contiguous United States constrained by S-to-P receiver functions. *Earth and Planetary Science Letters*, *495*(1), 79–86. https://doi.org/10.1016/j.epsl.2018.05.012

Lizarralde, D., Holbrook, W. S., & Oh, J. (1994). Crustal structure across the Brunswick magnetic anomaly, offshore Georgia, from coincident ocean bottom and multi-channel seismic data. *Journal of Geophysical Research*, *99*(B11), 21741–21757. https://doi.org/10.1029/94JB01550

Long, M. D., & Becker, T. W. (2010). Mantle dynamics and seismic anisotropy. *Earth and Planetary Science Letters*, *297*(3–4), 341–354. https://doi.org/10.1016/j.epsl.2010.06.036

Long, M. D., Benoit, M. H., Chapman, M. C., & King, S. D. (2010). Upper mantle anisotropy and transition zone thickness beneath southeastern North America and implications for mantle dynamics. *Geochemistry, Geophysics, Geosystems*, *11*(10), 1–22. https://doi.org/10.1029/2010GC003247

Long, M. D., Jackson, K. G., & McNamara, J. F. (2016). SKS splitting beneath Transportable Array stations in eastern North America and the signature of past lithospheric deformation. *Geochemistry, Geophysics, Geosystems*, *17*(1), 2–15. https://doi.org/10.1002/2015GC006088

Long, M. D., Wagner, L. S., King, S. D., Evans, R L., Mazza, S. E., Byrnes, J. S., et al. (2021). Evaluating models for lithospheric loss and intraplate volcanism beneath the Central Appalachian Mountains. *Journal of Geophysical Research*, *126*(10), e2021JB022571. https://doi.org/10.1029/2021JB022571

Lynner, C., & Bodmer, M. (2017). Mantle flow along the eastern North American margin inferred from shear wave splitting. *Geology*, *45*(10), 867–870. https://doi.org/10.1130/G38980.1

Lynner, C., & Porritt, R. W. (2017). Crustal structure across the eastern North American margin from ambient noise tomography. *Geophysical Research Letters*, *44*(13), 6651–6657. https://doi.org/10.1002/2017GL073500

Lynner, C., Van Avendonk, H. J. A., Bécel, A., Christeson, G. L., Dugan, B., Gaherty, J. B., et al. (2020). The eastern North American margin community seismic experiment: An amphibious active- and passive-source dataset. *Seismological Research Letters*, *91*(1), 533–540. https://doi.org/10.1785/0220190142

Marzen, R. E., Shillington, D. J., Lizarralde, D., Knapp, J. H., Heffner, D. M., Davis, J. K., & Harder, S. H. (2020). Limited and localized magmatism in the Central Atlantic Magmatic Province. *Nature Communications*, *11*, 1–8. https://doi.org/10.1038/s41467-020-17193-6

Maupin, V., & Park, J. (2007). Theory and observations – Wave propagation in anisotropic media. *Treatise on geophysics* (Vol. 1, pp. 289–321). Elsevier. https://doi.org/10.1016/B978-044452748-6.00007-9

Maus, S., Barckhausen, U., Berkenbosch, H., Bournas, N., Brozena, J., Childers, V., et al. (2009). EMAG2: A 2-arc min resolution Earth Magnetic Anomaly Grid compiled from satellite, airborne, and marine magnetic measurements. *Geochemistry, Geophysics, Geosystems*, *10*(8), Q08005. https://doi.org/10.1029/2009GC002471

Mazza, S. E., Gazel, E., Johnson, E. A., Kunk, M. J., McAleer, R., Spotila, J. A., & Coleman, D. S. (2014). Volcanoes of the passive margin: The youngest magmatic event in eastern North America. *Geology*, *42*(6), 483–486. https://doi.org/10.1130/G35407.1

McKenzie, D. (1978). Some remarks on the development of sedimentary basins. *Earth and Planetary Science Letters*, *40*(1), 25–32. https://doi.org/10.1016/0012-821X(78)90071-7

Menke, W. (2012). *Geophysical data analysis: Discrete inverse theory* (3rd ed.). Elsevier. https://doi.org/10.1016/C2011-0-69765-0

Menke, W., Skryzalin, P., Levin, V., Harper, T., Darbyshire, F., & Dong, T. (2016). The Northern Appalachian Anomaly: A modern asthenospheric upwelling. *Geophysical Research Letters*, *43*(19), 1–7. https://doi.org/10.1002/2016GL070918

Murphy, B. S., & Egbert, G. D. (2019). Synthesizing seemingly contradictory seismic and magnetotelluric observations in the southeastern United States to image physical properties of the lithosphere. *Geochemistry, Geophysics, Geosystems*, *20*(6), 2606–2625. https://doi.org/10.1029/2019GC008279

Pasyanos, M. E., Masters, T. G., Laske, G., & Ma, Z. (2014). LITHO1.0: An updated crust and lithospheric model of the Earth. *Journal of Geophysical Research: Solid Earth*, *119*(3), 2153–2173. https://doi.org/10.1002/2013JB010626

Penn State University. (2004). *Pennsylvania State Seismic Network [Data set]*. International Federation of Digital Seismograph Networks. https://doi.org/10.7914/SN/PE

Pollitz, F. F., & Mooney, W. D. (2016). Seismic velocity structure of the crust and shallow mantle of the Central and Eastern United States by seismic surface wave imaging. *Geophysical Research Letters*, *43*(1), 118–126. https://doi.org/10.1002/2015GL066637

Ramsay, T., & Pysklywec, R. (2011). Anomalous bathymetry, 3D edge driven convection, and dynamic topography at the western Atlantic passive margin. *Journal of Geodynamics*, *52*(1), 45–56. https://doi.org/10.1016/j.jog.2010.11.008

Rowley, D. B., Forte, A. M., Moucha, R., Mitrovica, J. X., Simmons, N. A., & Grand, S. P. (2013). Dynamic topography change of the Eastern United States since 3 million years ago. *Science*, *340*(6140), 1560–1563. https://doi.org/10.1126/science.1229180

Russell, J. B., Gaherty, J. B., Lin, P. Y. P., Lizarralde, D., Collins, J. A., Hirth, G., & Evans, R. L. (2019). High-resolution constraints on Pacific Upper mantle petrofabric inferred from surface-wave anisotropy. *Journal of Geophysical Research: Solid Earth*, *124*, 631–657. https://doi.org/10.1029/2018JB016598

Sandoval, S., Kissling, E., Ansorge, J., & SVEKALAPKO Seismic Tomography working Group. (2004). High-resolution body wave tomography beneath the SVEKALAPKO array - II. Anomalous upper mantle structure beneath the central Baltic Shield. *Geophysical Journal International*, *157*(1), 200–214. https://doi.org/10.1111/j.1365-246X.2004.02131.x

Sandwell, D. T., & Smith, W. H. F. (2009). Global marine gravity from retracked Geosat and ERS-1 altimetry: Ridge segmentation versus spreading rate. *Journal of Geophysical Research*, *114*(B1), B01411. https://doi.org/10.1029/2008JB006008

Savage, B. (2021). Body wave speed structure of eastern North America. *Geochemistry, Geophysics, Geosystems*, *22*, 1–18. https://doi.org/10.1029/2020GC009002

Savage, B., Covellone, B., & Shen, Y. (2017). Wave speed structure of the eastern North American margin. *Earth and Planetary Science Letters*, *459*, 394–405. https://doi.org/10.1016/j.epsl.2016.11.028

Schaeffer, A. J., Lebedev, S., & Becker, T. W. (2016). Azimuthal seismic anisotropy in the Earth's upper mantle and the thickness of tectonic plates. *Geophysical Journal International*, *207*, 901–933. https://doi.org/10.1093/gji/ggw309

Schlische, R. W. (2003). Progress in understanding the structural geology, basin evolution, and tectonic history of the eastern North American rift system *The great rift valleys of Pangea in eastern north America* (Vol. 1, pp. 21–64). Columbia University Press. https://doi.org/10.7312/leto11162-003

Schmandt, B., & Humphreys, E. (2010). Seismic heterogeneity and small-scale convection in the southern California upper mantle. *Geochemistry, Geophysics, Geosystems*, *11*(5), 1–19. https://doi.org/10.1029/2010GC003042

Schmandt, B., & Lin, F. (2014). P and S wave tomography of the mantle beneath the United States. *Geophysical Research Letters*, *41*(18), 6342–6349. https://doi.org/10.1002/2014GL061231

Shahnas, M. H., & Pysklywec, R. N. (2004). Anomalous topography in the western Atlantic caused by edge-driven convection. *Geophysical Research Letters*, *31*, L18611. https://doi.org/10.1029/2004GL020882

Shen, W., & Ritzwoller, M. H. (2016). Crustal and uppermost mantle structure beneath the United States. *Journal of Geophysical Research: Solid Earth*, *121*(6), 4306–4342. https://doi.org/10.1002/2016JB012887

Shillington, D. J., Holbrook, W. S., Van Avendonk, H. J., Tucholke, B. E., Hopper, J. R., Louden, K. E., et al. (2006). Evidence for asymmetric nonvolcanic rifting and slow incipient oceanic accretion from seismic reflection data of the Newfoudland margin. *Journal of Geophysical Research*, *111*(9), B09402. https://doi.org/10.1029/2005JB003981

Shuck, B., & Van Avendonk, H. J. (2016). *Evolution of the upper lithosphere in the ENAM area from 3-D wide-angle seismic data*. AGUFM. T51G–2998S.

Shuck, B. D., Van Avendonk, H. J., & Bécel, A. (2019). The role of mantle melts in the transition from rifting to seafloor spreading offshore eastern North America. *Earth and Planetary Science Letters*, *525*, 115756. https://doi.org/10.1016/j.epsl.2019.115756

Silver, P. G. (1996). Seismic anisotropy beneath the continents: Probing the depths of geology. *Annual Review of Earth and Planetary Sciences*, *24*, 385–432. https://doi.org/10.1146/annurev.earth.24.1.385

Silver, P. G., & Chan, W. W. (1991). Shear wave splitting and subcontinental mantle deformation. *Journal of Geophysical Research*, *96*(B10), 16429–16454. https://doi.org/10.1029/91jb00899

Skemer, P., & Hansen, L. N. (2016). Inferring upper-mantle flow from seismic anisotropy: An experimental perspective. *Tectonophysics*, *668–669*, 1–14. https://doi.org/10.1016/j.tecto.2015.12.003

Skemer, P., Warren, J. M., & Hirth, G. (2012). The influence of deformation history on the interpretation of seismic anisotropy. *Geochemistry, Geophysics, Geosystems*, *13*(3), 1–10. https://doi.org/10.1029/2011GC003988

Suárez, G., van Eck, T., Giardini, D., Ahern, T., Butler, R., & Tsuboi, S. (2008). The international federation of digital seismograph networks (FDSN): An integrated system of seismological observatories. *IEEE Systems Journal*, *2*(3), 431–438. https://doi.org/10.1109/JSYST.2008.2003294

Takeo, A., Kawakatsu, H., Isse, T., Nishida, K., Sugioka, H., Ito, A., & Suetsugu, D. (2016). Seismic azimuthal anisotropy in the oceanic lithosphere and asthenosphere from broadband surface wave analysis of OBS array records at 60 Ma seafloor. *Journal of Geophysical Research: Solid Earth*, *121*(3), 1927–1947. https://doi.org/10.1002/2015JB012429

Tao, Z., Li, A., & Fischer, K. M. (2021). Hotspot signatures at the North American passive margin. *Geology*, *49*(5), 525–530. https://doi.org/10.1130/G47994.1

Tommasi, A., Tikoff, B., & Vauchez, A. (1999). Upper mantle tectonics: Three-dimensional deformation, olivine crystallographic fabrics and seismic properties. *Earth and Planetary Science Letters*, *168*(1–2), 173–186. https://doi.org/10.1016/S0012-821X(99)00046-1

University of Memphis. (1982). *CERI Southern Appalachian Seismic Network*. https://www.fdsn.org/networks/detail/ET/

University of South Carolina. (1987). *South Carolina Seismic Network [Data set]*. International Federation of Digital Seismograph Networks. https://doi.org/10.7914/SN/CO

University of South Carolina. (2000). *South Carolina Earth Physics Project [Data set]*. International Federation of Digital Seismograph Networks. https://doi.org/10.7914/SN/SP

Van Avendonk, H. J. A., Holbrook, W. S., Nunes, G. T., Shillington, D. J., Tucholke, B. E., Louden, K. E., & Hopper, J. R. (2006). Seismic velocity structure of the rifted margin of the eastern Grand Banks of Newfoundland, Canada. *Journal of Geophysical Research*, *111*, B11404. https://doi.org/10.1029/2005JB004156

VanDecar, J. C., & Crosson, R. S. (1990). Determination of teleseismic relative phase arrival times using multi-channel cross-correlation and least squares. *Bulletin of the Seismological Society of America*, *80*(1), 150–169.

van der Lee, S., Regenauer-Lieb, K., & Yuen, D. A. (2008). The role of water in connecting past and future episodes of subduction. *Earth and Planetary Science Letters*, *273*(1–2), 15–27. https://doi.org/10.1016/j.epsl.2008.04.041

Vauchez, A., Tommasi, A., & Barruol, G. (1998). Rheological heterogeneity, mechanical anisotropy and deformation of the continental lithosphere. *Tectonophysics*, *296*(1–2), 61–86. https://doi.org/10.1016/S0040-1951(98)00137-1

Vauchez, A., Tommasi, A., Barruol, G., & Maumus, J. (2000). Upper mantle deformation and seismic anisotropy in continental rifts. *Physics and Chemistry of the Earth - Part A: Solid Earth and Geodesy*, *25*(2), 111–117. https://doi.org/10.1016/S1464-1895(00)00019-3

Vine, F. J., & Mathews, D. H. (1963). Magnetic anomalies over oceanic ridges. *Nature*, *199*(4897), 947–949. https://doi.org/10.1038/199947a0

Wagner, L. (2009). *Appalachian Seismic Transect [Data set]*. International Federation of Digital Seismograph Networks. https://doi.org/10.7914/SN/Z4_2009

Wagner, L. (2012). *Pre-Hydrofracking Regional Assessment of Central Carolina Seismicity [Data set]*. International Federation of Digital Seismograph Networks. https://doi.org/10.7914/SN/XQ_2012

Wagner, L. S., Fischer, K. M., Hawman, R., Hopper, E., & Howell, D. (2018). The relative roles of inheritance and long-term passive margin lithospheric evolution on the modern structure and tectonic activity in the southeastern United States. *Geosphere*, *14*(4), 1385–1410. https://doi.org/10.1130/GES01593.1

Wagner, L. S., Long, M. D., Johnston, M. D., & Benoit, M. H. (2012). Lithospheric and asthenospheric contributions to shear-wave splitting observations in the southeastern United States. *Earth and Planetary Science Letters*, *341–344*, 128–138. https://doi.org/10.1016/j.epsl.2012.06.020

Wang, H., Zhao, D., Huang, Z., & Wang, L. (2019). Tomography, seismotectonics, and mantle dynamics of central and eastern United States. *Journal of Geophysical Research: Solid Earth*, *124*(8), 8890–8907. https://doi.org/10.1029/2019JB017478

Wang, W., & Becker, T. W. (2019). Upper mantle seismic anisotropy as a constraint for mantle flow and continental dynamics of the North American plate. *Earth and Planetary Science Letters*, *514*, 143–155. https://doi.org/10.1016/j.epsl.2019.03.019

Wernicke, B. (1985). Uniform-sense normal simple shear of the continental lithosphere. *Canadian Journal of Earth Sciences*, *22*(1), 108–125. https://doi.org/10.1139/e85-009

Withjack, M. O., & Schlische, R. W. (2005). A review of tectonic events on the passive margin of eastern North America. In *Petroleum systems of divergent continental margin basins* (pp. 203–235). SEPM Society for Sedimentary Geology. https://doi.org/10.5724/gcs.05.25.0203

Withjack, M. O., Schlische, R. W., & Olsen, P. E. (2012). Development of the passive margin of eastern North America: Mesozoic rifting, igneous activity, and breakup. In *Regional geology and tectonics: Phanerozoic rift systems and sedimentary basins* (pp. 301–335). Elsevier. https://doi.org/10.1016/B978-0-444-56356-9.00012-2

Wolfe, C. J., & Solomon, S. C. (1998). Shear-wave splitting and implications for mantle flow beneath the MELT region of the east Pacific Rise. *Science*, *280*(5367), 1230–1232. https://doi.org/10.1126/science.280.5367.1230

Worthington, L., Shuck, B., Becel, A., Eilon, Z., & Lynner, C. (2021). Breaking up is hard to do, especially for continents. *Eos*, *102*. https://doi.org/10.1029/2021EO155889

Yang, B. B., Liu, Y., Dahm, H., Liu, K. H., & Gao, S. S. (2017). Seismic azimuthal anisotropy beneath the eastern United States and its geodynamic implications. *Geophysical Research Letters*, *44*(6), 2670–2678. https://doi.org/10.1002/2016GL071227

Yuan, H., Romanowicz, B., Fischer, K. M., & Abt, D. (2011). 3-D shear wave radially and azimuthally anisotropic velocity model of the North American upper mantle. *Geophysical Journal International*, *184*(3), 1237–1260. https://doi.org/10.1111/j.1365-246X.2010.04901.x

Yuan, X., Heit, B., Brune, S., Steinberger, B., Geissler, W. H., Jokat, W., & Weber, M. (2017). Seismic structure of the lithosphere beneath NW Namibia: Impact of the Tristan da Cunha mantle plume. *Geochemistry, Geophysics, Geosystems*, *18*(1), 125–141. https://doi.org/10.1002/2016GC006645

Zelt, C. A. (1998). Lateral velocity resolution from three-dimensional seismic refraction data. *Geophysical Journal International*, *135*(3), 1101–1112. https://doi.org/10.1046/j.1365-246X.1998.00695.x

Zhang, S., & Karato, S.-i. (1995). Lattice preferred orientation of olivine aggregates deformed in simple shear. *Nature*, *375*(6534), 774–777. https://doi.org/10.1038/375774a0

Ziegler, P. A., & Cloetingh, S. (2004). Dynamic processes controlling evolution of rifted basins. *Earth-Science Reviews*, *64*, 1–50. https://doi.org/10.1016/S0012-8252(03)00041-2

References From the Supporting Information

Rawlinson, N., & Spakman, W. (2016). On the use of sensitivity tests in seismic tomography. *Geophysical Journal International*, *205*, 1221–1243. https://doi.org/10.1093/gji/ggw084

Rickers, F., Fichtner, A., & Trampert, J. (2013). The Iceland-Jan Mayen plume system and its impact on mantle dynamics in the North Atlantic region: Evidence from full-waveform inversion. *Earth and Planetary Science Letters*, *367*, 39–51. https://doi.org/10.1016/j.epsl.2013.02.022